Applied Surface Science 665 (2024) 160320

Contents lists available at ScienceDirect

Applied Surface Science

journal homepage: www.elsevier.com/locate/apsusc

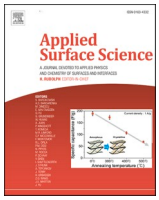

Full Length Article

Thermal-induced evolution of microstructure as a plasma arc coating Direction-Dependent phenomenon

Augustine Nana Sekyi Appiah [a,*], Gilmar Ferreira Batalha [b], Marcin Adamiak [a]

[a] Materials Research Laboratory, Faculty of Mechanical Engineering, Silesian University of Technology, 18A Konarskiego Street, 44-100 Gliwice, Poland
[b] Department of Mechatronics and Mechanical Systems Engineering, Polytechnic School of Engineering of the University of Sao Paulo (USP), São Paulo 05508-900, Brazil

ARTICLE INFO

Keywords:
NiCrBSi Coatings
Finite Element Method
Microstructural Examination
Electron Backscatter Diffraction
Corrosion Resistance
Electrochemical Impedance Spectroscopy
Wear Resistance

ABSTRACT

This study elucidates the effects of different directed energy deposition trajectories on the microstructure and properties of powder plasma transferred arc welding (PPTAW) fabricated coatings. Two trajectories, straight (STT) and complex (CXT), were explored to deposit NiCrBSi powders onto a low alloy steel substrate. Finite element thermal analysis revealed distinct heat distribution zones, the middle zone (MZ) and transition zone (TZ), showing temperature variations between the STT and CXT coatings. Microstructural examination indicated lower dendrite arm spacing (DAS) in the STT coating (11 μm) than in the CXT coating (16 μm). Electron backscatter diffraction (EBSD) analysis demonstrated significant grain refinement in the STT coating (17.4 μm) versus the CXT coating (68.7 μm). X-ray diffraction phase analysis identified three reinforcing phases – γ-Ni, $Cr_{23}C_6$, and Cr_3C_2 – enhancing corrosion resistance and tribological properties. The STT coating exhibited superior corrosion resistance with a corrosion current density (i_{corr}) of 12.8 μA/cm^2, while the CXT coating showed i_{corr} of 34.3 μA/cm^2. Additionally, the STT coating exhibited higher hardness (832 ± 33 $HV_{1.0}$) and better wear resistance with a wear rate of 10.46 ± 0.29 × 10^{-3} m^3/m, over the CXT coating (hardness: 450 ± 36 $HV_{1.0}$; wear rate: 12.67 ± 0.54 × 10^{-3} m^3/m).

1. Introduction

Directed energy deposition (DED) techniques, such as laser cladding (LC), and plasma transferred arc welding (PTAW), have gained significant attention in industrial applications for preparing surface layers aimed at prolonging the service lives of structural components. The escalating demand for tools, machine components, and parts exhibiting enhanced resistance to wear, and corrosion has spurred interest in these techniques [1–4]. PTAW has recently seen increased adoption and industrial utilization for demanding wear and corrosion applications. The growing adoption of PTAW is fueled by its ability to achieve precise material deposition and exert control over coating microstructures using only a single coating layer [5]. For example, Adamiak et al. [6] recently conducted an experimental comparison between LC and PTAW for depositing a WC-reinforced composite onto a structural steel substrate. The results demonstrated that the PTAW approach produced a more homogenized microstructure with superior tribological properties relative to the LC approach. The relatively high thermal cycles (heating and cooling rates) of the PTAW process enable the precipitation of phases that prove more pragmatic for specific applications. In a study by Habib et al. [7], focusing on the deposition of NiCrBSi coatings using high-velocity oxyfuel (HVOF), the phase evolution comprised a γ-Ni solid solution with minor Ni_3B and CrB phases. Conversely, when Wang et al. [8] used LC for deposition of NiCrBSi coatings, the evolved phases included metastable Ni_3B eutectics and precipitates of CrB and Cr_3C_2 or $(Cr, Fe)_7C_3$. However, when PTAW was used by Wanare et al. [9] to deposit the same material, the evolved phases comprised the $M_{23}C_6$ (M = Cr in this case) phase within the γ-Ni solid solution. This $M_{23}C_6$ phase is characterized by enhanced corrosion resistance and excellent tribological properties [10,11].

Similar to the evolved and precipitated phases, the microstructure of coatings plays a pivotal role in determining their performance. Chen et al. [12] identified instances of hot cracking in the middle zone (MZ) of Ni-based coatings, attributed to the presence of topologically closed-packed eutectic phases originating from dilution during coating solidification. Luiz et al. [13] found a notable decline in the corrosion resistance of their investigated coatings upon solidification. This decline was linked to the existence of interdendritic precipitates and a high Fe content in the coating MZ, leading to the initiation of galvanic corrosion.

* Corresponding author.
E-mail address: augustine.appiah@polsl.pl (A.N.S. Appiah).

https://doi.org/10.1016/j.apsusc.2024.160320
Received 30 January 2024; Received in revised form 13 May 2024; Accepted 17 May 2024
Available online 18 May 2024

Nomenclature

Q_f	Generated heat at fore of heat source (W)
Q_r	Generated heat at rare of heat source (W)
V	Voltage (V)
I	Current (A)
$x, y, z,$	Coordinates (m)
f_f	Distribution coefficient at fore of heat source
f_r	Distribution coefficient at rare of heat source
T	Temperature (K)
$Q(x,y,z)$	Heat flux (Wm^{-2})
$abc_{f,r}$	Coordinates at fore and rare of ellipsoid (m)
GTA	Grain tolerance angle (°)
DGS	Dendritic Growth Solidification (μm)
T_{max}	Maximum temperature (°C)
H	Vickers Microhardness (HV)
L_s	Sliding distance (m)
STT	Straight DED trajectory
CGHAZ	Coarse grained heat-affected zone (μm)
LAGB	Low angle grain boundary
EIS	Electrochemical Impedance Spectroscopy
SEM	Scanning electron microscopy
EBSD	Electron backscatter diffraction
t	Time (s)
Z'	Real part of Nyquist complex plane (Ωcm^2)
Z''	Imaginary part of Nyquist complex plane (Ωcm^2)
i_{corr}	Corrosion current density ($\mu A/cm^2$)
E_{corr}	Corrosion potential (mV)
E_{ocp}	Open circuit potential (mV vs. Ag/AgCl)
R_{ct}	Charge transfer resistance (Ωcm^2)
F	Frequency (Hz)
ΔH_f	Enthalpy of formation ($kJmol^{-1}$)
G	Gibbs free energy (J)
PGS	Planar growth solidification (μm)
CDGS	Cellular dendritic growth solidification (μm)
CR	Cooling rate (K/s)
W	Applied wear load (N)
V_s	Volume loss (m^3)
CXT	Complex DED trajectory
IPF	Inverse pole figure
HAGB	High angle grain boundary
LOM	Light optical microscopy
EDS	Energy dispersive X-ray spectroscopy
XRD	X-ray diffraction

Similar structural disparities are evident in the coating/substrate interface, influencing the coatings' performance and stability. Structural consideration at the coating/substrate interface is crucial to understanding the resulting properties and performance of the prepared coatings, especially considering it is the site where the coating-substrate bonding is established. The interface is particularly susceptible to hydrogen embrittlement, as noted by Kim et al. [14]. Hydrogen embrittlement is associated with the coating's susceptibility to brittleness resulting from the interface's higher hardness, especially at the HAZ, coupled with the presence of macrosegregations that are partially diluted and occur over a chemical composition gradient. The interface may also feature a type-II boundary – a high-angle grain boundary typically parallel to the coating/substrate interface transition zone (TZ) [15], which has been identified as a potential site for sulfide stress corrosion cracking in the coating [16].

Protective coatings prepared via PTAW are usually deposited using two main deposition techniques. One approach involves deposition along the longitudinal section of the substrate material through multiple passes until complete coverage is achieved, known as the straight trajectory (STT) or x–path method. Studies such as that conducted by Zheng et al. [17] and Farias et al. [18] adopted this method for their PTAW sample preparation. The alternative method entails applying coatings in the short transverse direction of the substrate material through several passes until the entire surface is coated, referred to as the complex trajectory (CXT) or the y–path method. Studies involving the use of this deposition trajectory for sample preparation can also be seen in the literature [19–21]. As PTAW technology progresses, research has delved into various aspects, including the selection of coating materials [22–24], heat evolution during the process [25–27], parameter optimization [28–30], and post-processing [31]. However, recently, researchers have observed variations in the performance of coatings produced by high energy density processes such as PTAW, emanating from the type of deposition trajectory used. This insight has been gained through a combination of experimental analyses and numerical trajectory-specific optimizations, highlighting the influence of deposition trajectory on the resulting coating properties [32–36]. In a notable study, Kim et al. [37] investigated the impact of these plasma-assisted DED trajectories on the mechanical properties of Inconel 718 when deposited onto a SUS304L steel substrate. The study employed STT, CXT, and a hybrid STT-CXT approach for sample preparation. The results indicated that the STT sample demonstrated superior hardness, yield strength, ultimate tensile strength, and elongation. The hybrid STT-CXT sample closely followed, but its extended sample preparation time rendered it impractical for applicable adoption. Conversely, the CXT sample exhibited the least favorable mechanical properties among the tested samples.

Despite the existing body of research, a comprehensive understanding of the relationship between deposition trajectories, microstructure, corrosion, and tribological properties of plasma DED coatings still represents a significant gap in knowledge. Since most of these coatings aim to improve the corrosion resistance and tribological properties of the substrate materials, acquiring knowledge to address this gap in the literature is essential. Therefore, the objective of this study is to elucidate the distinctions between the two PTAW processing trajectories, STT and CXT. The novelty lies in adopting a hybrid computational-experimental approach to unravel the interplay between trajectory-induced microstructural effects on the evolution of the interface and its thermal behavior, as well as the hardness, corrosion, and wear properties of coatings prepared using each trajectory, which is lacking in the current literature. To reach this goal, performance investigations are conducted through corrosion resistance tests – EIS and potentiodynamic tests, microhardness tests, wear resistance tests, and the characterization of microstructure and crystallography using LOM, stereoscopic microscopy, SEM, EDS, EBSD, and XRD techniques.

2. Methodology

2.1. PPTAW sample preparation

The powder plasma transferred arc welding (PPTAW) system utilized in this investigation is the Castolin Eutectic GAP 2001 DC machine. The working principle of this system is illustrated in Fig. 1**(a)**. The plasma arc control unit (Eutronic) is equipped with a reservoir containing Argon 5.0 with 99.99 % purity (ISO 14175-I1:2009). As a shielding and carrier gas, a mixture of argon and hydrogen (5 % H_2, Ar) in accordance with the ISO 14175-R1-ArH-5 welding mixture was used.

Two deposition techniques were used to prepare the samples, and these formed the basis for this study. The first technique involved deposition using a straight trajectory (STT). In this method, surface layers were deposited longitudinally on the substrate material as

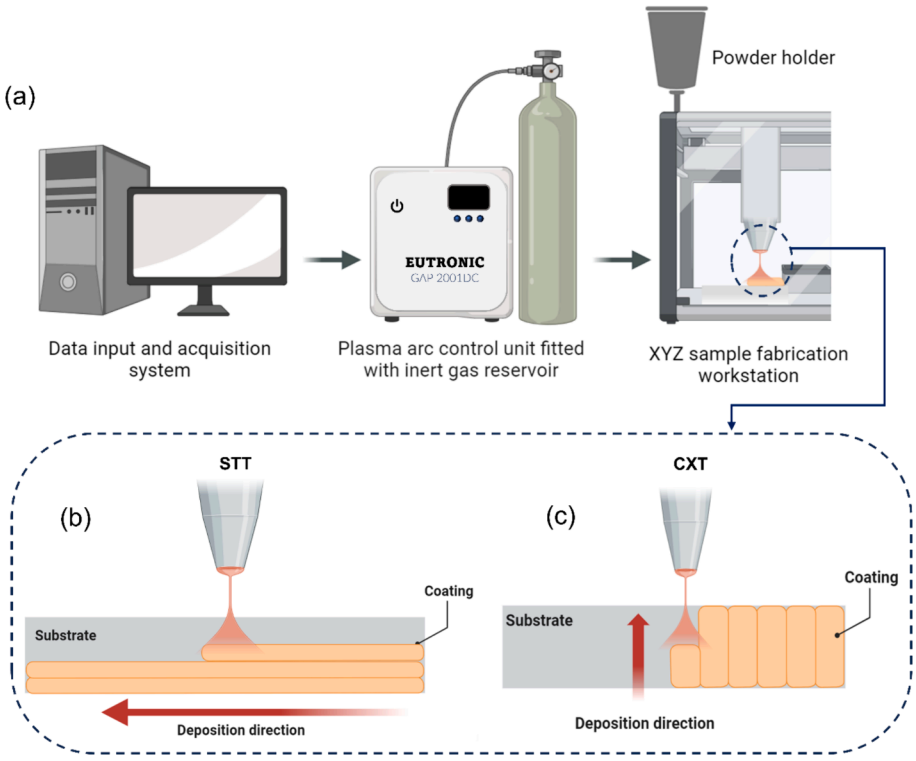

Fig. 1. **(a)** Workflow schematic of the PPTAW system **(b)** Straight trajectory (STT) deposition technique **(c)** Complex trajectory (CXT) deposition technique.

depicted in Fig. 1**(b).** This approach introduced a relatively higher amount of powder during the coating process, and after four STT passes with a 30 % inter-pass overlap, the surface of the steel plate was completely covered by the coatings.

The second technique was deposition using a complex trajectory (CXT). Coatings in this technique were deposited by moving the plasma torch in the short transverse direction on the substrate surface as illustrated in Fig. 1**(c).** The CXT technique achieved full coating on the substrate material's surface after 18 passes with a 30 % inter-pass overlap.

Fig. 2 provides a schematic illustration of the plasma torch, serving as the cathode through which powders are fed. The torch features a centrally positioned tungsten electrode (WS-2) that generates the plasma arc. The process conditions for the PPTAW process used in this study are summarized in Table 1, whereas Fig. 3 shows a view of the PPTAW system in the laboratory.

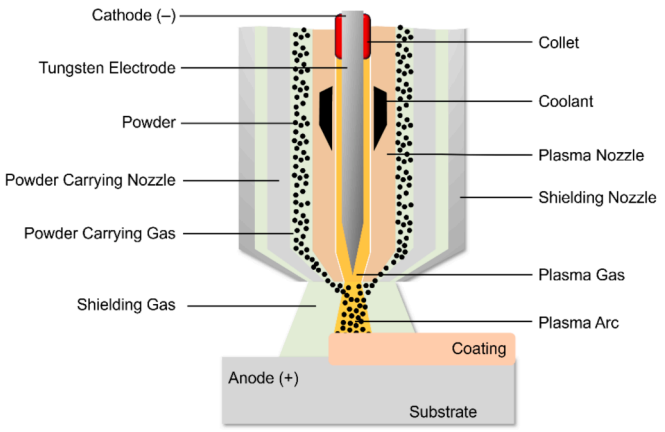

Fig. 2. Schematic diagram of the plasma torch.

Table 1
PPTAW process conditions.

Parameter	Value	Unit
Electrode diameter	4	mm
Plasma nozzle size	2	mm
Plasma arc current	70	A
Plasma gas flow rate	2.0	L/min
Travel speed	2.0	mm/s
Standoff distance	8	mm
PTA thermal coefficient	0.6	

2.2. Materials

NiCrBSi powder (Durmat 456) was used for this research. This powder, prepared by gas atomization, exhibited predominantly spherical particles under the SEM, depicted in Fig. 4**A**. Laser-assisted particle size analysis (Fig. 4**B**) yielded a particle diameter (d_{90}) of 126 μm, with a computed dimensionless factor, span, registering at 1.6. A span of 1 indicates complete particle uniformity, with higher values denoting decreased uniformity [38]. The observed span of 1.6 implies a good level of particle uniformity and suitability for the process [39]. Its chemical composition obtained from EDS analysis is detailed in Fig. 4**C**.

The base material for this investigation was 15HM steel, a common alloy in industries such as petroleum chemistry, valued for its high wear and corrosion resistance at elevated temperatures. This low-alloy steel has been a subject of several studies aimed at prolonging its service life in relevant applications [40–42]. Its microstructure, illustrated in Fig. 4**D** under an optical microscope, reveals a pearlitic-ferritic structure, with quasi-polygonal ferrite phases constituting around 60 % and pearlitic constituents around 40 %. The measured Vickers microhardness of the material's cross-section is approximately 152 ± 5 HV (Fig. 4**E**). The base material's chemical composition obtained from EDS analysis is presented in Fig. 4**F**.

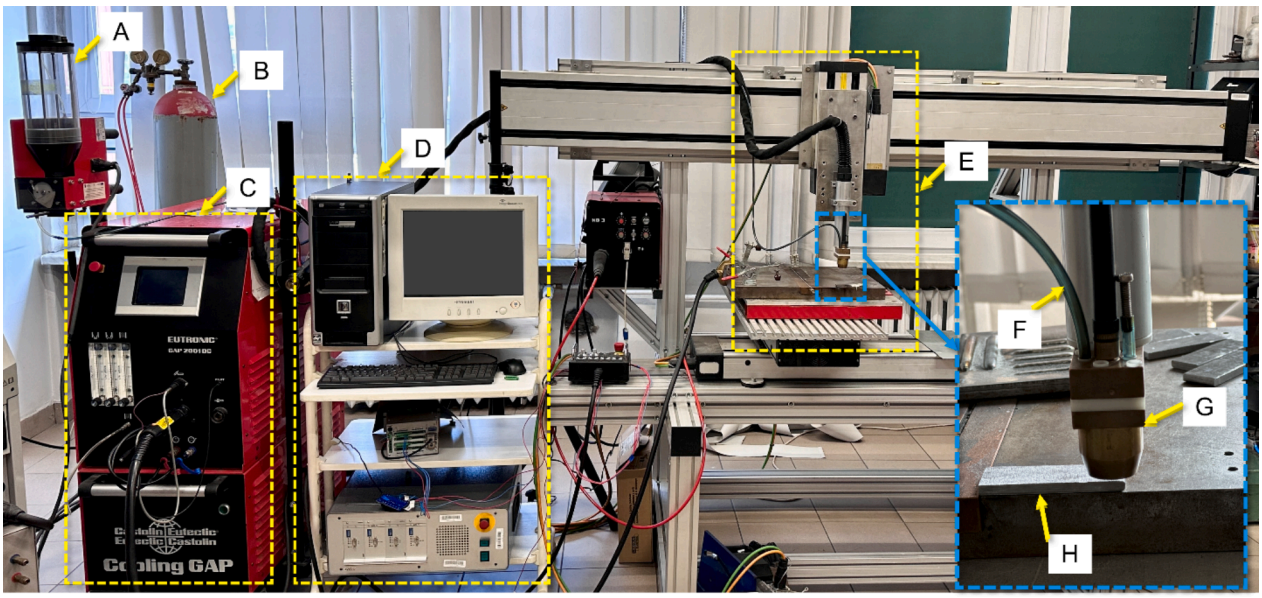

Fig. 3. View of the GAP 2001 DC surfacing machine used for sample preparation. **A.** Powder holder, **B.** Inert gas reservoir, **C.** Control unit, **D.** Data input and acquisition system, **E.** XYZ robotic arm and workpiece table, **F.** Powder feeder, **G.** E52 plasma torch, and **H.** Substrate material.

2.3. Thermal analyses

3D non-linear transient finite element method, using ESI VisualWeld 16.0 (SYSWELD core) was used to perform thermal analyses. The purpose of this approach was to provide a basis for understanding the evolution of heat during PPTAW sample preparation using the different deposition methods. The PPTAW process was represented by the double ellipsoidal Gaussian distribution heat source model given in **Eq. (1)** [43].

$$Q_{f,r}(x,y,z,t) = \frac{6\sqrt{3}f_{f,r}Qn}{abc_{f,r}\prod^{3/2}} exp\left[-3\left\{\left(\frac{x}{a}\right)^2 + \left(\frac{y}{b}\right)^2 + \left(\frac{z+v(\tau-t)}{c_{f,r}}\right)^2\right\}\right] \quad (1)$$

$f_{f,r}$ signifies the proportional coefficient governing the distribution of heat at the front and rear of the heat source, individually, and its computation is determined by the following formula.

$$f_f = \frac{2c_r}{C_r + C_f} \text{and} f_r = \frac{2c_f}{C_f + C_r}$$

The initial boundary conditions involve assessing the temperature distribution across all components of the specimen at ambient conditions before the commencement of the PPTAW process. This is expressed by **Eq. (2)**.

$$T = 25^{\circ}C at t = 0s \quad (2)$$

The examination of the substrate steel plate's thermal properties involved the imposition of boundary conditions on its upper, lateral, and lower surfaces. The intention behind this methodology was to replicate the heat dissipation characteristics witnessed in the conducted experiment. Thermal restrictions on the upper and lateral surfaces were imposed through convective and radiative loss mechanisms. In contrast, the lower surface of the plate underwent a distinctive thermal limitation, establishing direct thermal connectivity with a heatsink. The thermal linkage was characterized by a thermal resistance value of 10 x 10^{-4} (Wm^2)/K, deliberately chosen to simulate the low-pressure thermal contact conditions observed in the experimental configuration, as illustrated in Fig. 3**(G and H)**.

Table 2 presents the thermo-mechanical properties of the deposited powder and the base material, used for numerical simulations.

2.4. Characterization

Metallographic samples intended for analyses underwent a preparation procedure, which included grinding using SiC sheets ranging from 200 to 2000 grit size, and polishing with colloidal silica with a particle size of 0.04 μm. For microstructural characterization, Zeiss LOM and SEM fitted with an EDS system (EVO 15 MA) were utilized. EBSD was used for grain size and crystallographic analyses by setting the step size to 0.2 μm at a voltage of 20 kV.

X-ray diffraction (XRD) analysis was carried out using the PANalytical X'Pert Pro diffraction system manufactured by Panalytical B.V. (currently known as Malvern Panalytical Ltd.) in Almelo, The Netherlands. A cobalt anode lamp (KαCo λ = 0.179 nm) was utilized, operating at a voltage of 40 kV with a filament current intensity of 30 mA. The measurements were conducted in the Bragg–Brentano geometry, spanning an angular range of 20° – 110° 2θ, with a step size of 0.05° and a step count time of 100 s. Subsequently, the obtained diffractograms underwent analysis using the X'Pert High Score Plus software (version 3.0e), coupled with the dedicated Inorganic Crystal Structure Database (ICSD) from FIZ, Karlsruhe, Germany.

2.5. Corrosion tests

The assessment of corrosion resistance was conducted through potentiodynamic testing, wherein anodic polarization curves were recorded. The test configuration constituted an Atlas 0531 EU potentiostat and a standard three – electrode system at room temperature in a 3.5 % NaCl aqueous solution. A platinum-based PtP-201 electrode and an Ag/AgCl electrode were used as auxiliary and reference electrodes respectively. After an open circuit potential (E_{ocp}) stabilization period of 3600 s, the corrosion testing was initiated. Subsequently, by using a scan rate of 0.375 mVs^{-1} and **Eq. (3)** to measure the potential, anodic polarization curves were generated.

$$E_{start} = E_{ocp} - 100mV \quad (3)$$

The tests ended with a 2 V potential (E_{final}), after which there was a reversal in polarity to record the curves returning to E_{start}. By using the Tafel approach, i_{corr} and E_{corr} were estimated, aided by the AtlasLab software. EIS experiments were carried out using the sample potentiostat and NaCl aqueous solution kept at the free potential. The signal

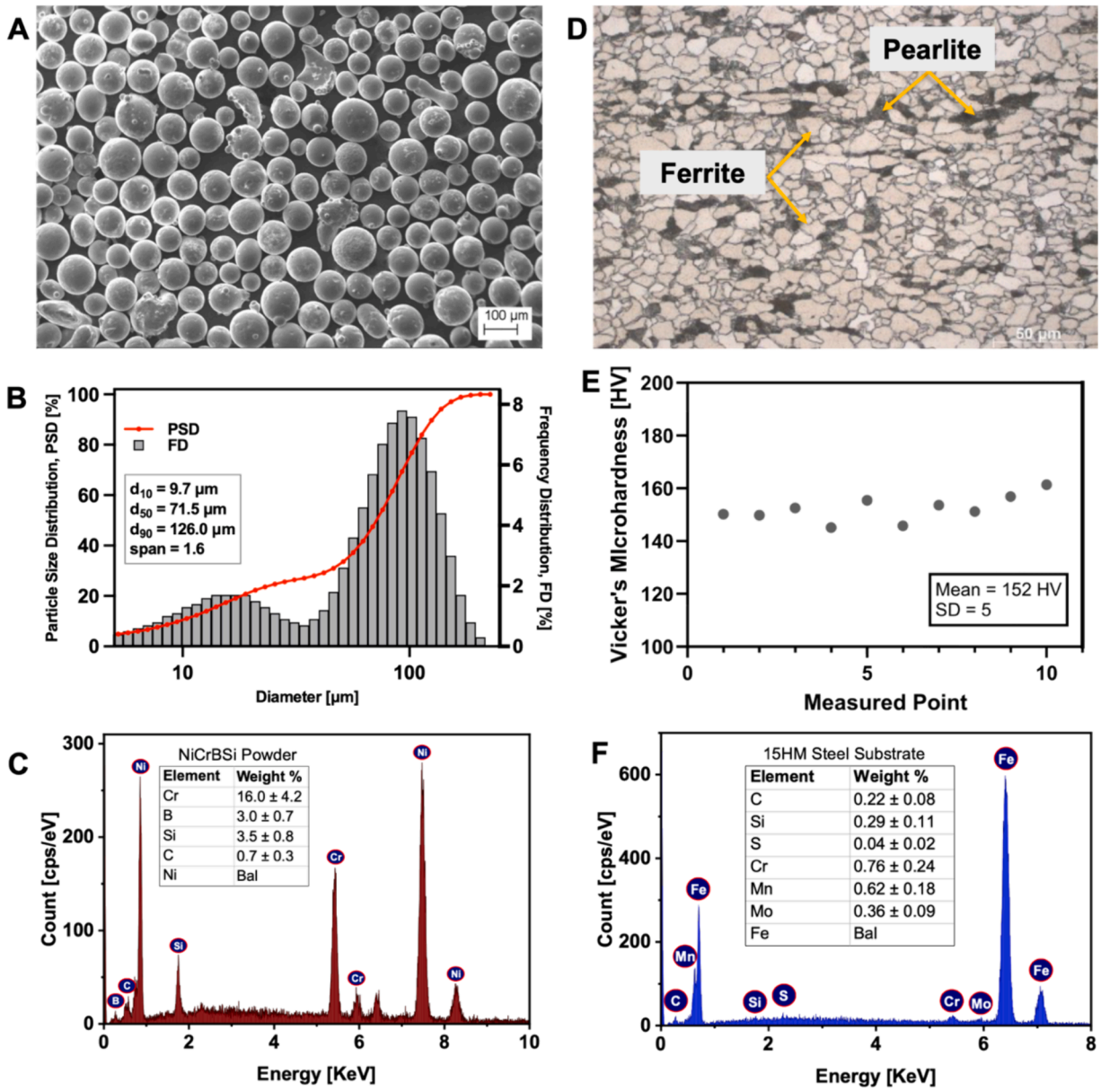

Fig. 4. Materials for sample preparation. A. Morphology of NiCrBSi powders used for coating preparation, **B.** Powder particle size analysis, **C.** Chemical composition of the deposited powder (weight %), **D.** Optical micrograph of the substrate material, **E.** Vicker's microhardness of substrate material, and **F.** Chemical composition of substrate material (weight %).

Table 2
Thermo-mechanical properties of the deposited powder and the substrate material used for numerical thermal analysis.

Parameters	Range	Unit	Temperature range [°C]
NiCrBSi powder			
Specific heat	410–970	J/(kg • K)	0–1000
Density	8040–7500	Kg/m^3	0–1000
Thermal conductivity	9.2–17.5	W/(m • K)	0–1000
Melting point	1000	°C	
15HM Steel			
Specific heat	483–1349	J/(kg • K)	0–1500
Density	7815–7290	Kg/m^3	0–1500
Thermal conductivity	39–24	W/(m • K)	0–1500
Melting point	1500	°C	

amplitude was 10 mV and the test covered a frequency range of 100 kHz – 10 mHz.

2.6. Tribological investigations

The CSM tribometer (Switzerland) was used to assess the coefficient of friction through a ball-on-disc technique. The counter specimen was a 6 mm – diameter zirconium oxide (ZrO_2) G28 ball with a marked minimum hardness of approximately 940 HV. The normal load was 30 N and the test duration was 3000 s, corresponding to a sliding distance of 77 m. A 2.0 Hz frequency was maintained for all tested specimens. The wear tests were repeated three times for each specimen and the average values of the investigated parameters were reported. The microhardness (Vickers) of the specimens was measured using the FM – ARS 9000 microhardness instrument (FTC, Tokyo). The test load was 9.8 N.

3. Results and discussions

3.1. Interface

Fig. 5**(a)** presents the overview of the interface of the STT sample. Fig. 5**(b)** illustrates the solidification modes of the coating produced through the STT method, revealing a two-stage process: planar growth solidification (PGS) followed by dendritic growth solidification (DGS). The heat-affected zone (HAZ) depicted in Fig. 5**(c)** exhibits coarse grains, identified as coarse-grained heat-affected zone (CGHAZ), composed of lath martensite (M). Additionally, a small peninsula-like macrosegregation is seen, as marked by the ellipse in Fig. 5**(d)**.

Fig. 6**(a)** displays the interface overview of the CXT sample. The solidification process in this sample proceeds in three stages (Fig. 6**(b)**): cellular dendritic growth solidification (CDGS), PGS, and terminates with DGS. The HAZ in this scenario (Fig. 6**(c)**) mirrors the CGHAZ observed in the STT sample. A closer examination of the CDGS region reveals interdendritic precipitates rich in Cr (Fig. 6**(d)**). Furthermore, the CXT sample displays type-II boundaries at the interface (Fig. 6**(e)**).

Comparing the SEM images, the transition zone (TZ) at the interface of the STT sample is thinner, measuring approximately 13 μm, while the CXT sample's interface exhibits a larger TZ, around 21 μm. A notable distinction lies in the absence of discontinuities in the STT's TZ, whereas the CXT's TZ is preceded by a CDGS region. Both coatings appear to exhibit metallurgical bonding with the substrate, although they undergo solidification through different modes. The difference in solidification modes (PGS-DGS for STT and CDGS-PGS-DGS for CXT) can be attributed to the instability of the solid–liquid interface induced by substrate heating during the coating process [44]. Another possible phenomenon that can account for this transition in the solidification modes is constitutional supercooling, which is defined as the reduction in the solubility of the solid relative to the liquid [45]. The CDGS growth mode stems from the competitive growth of the grains in the weld pool. The grains possessing relatively higher growth rates tend to impede the growth of their neighbors, creating an oriented microstructure. The observed CDGS at the interface of the CXT specimen results from an intense nucleation rate, facilitated by the substrate's heat sink and numerous nucleation sites. This is because partially melted powder particles at the interface have been reported to also act as nucleation sites [46]. The interdendritic precipitates in the CDGS are fine and discontinuous, signifying good weldability based on the criterion proposed by Sudhagar et al. [47].

Unique to the STT sample, tiny peninsula-like macrosegregations are observed. This phenomenon is attributed to the presence of a stagnated substrate liquid layer, indicating less melted substrate material [48]. This results from the dissimilarities between the fusion temperatures of the base material and that of the deposited powder, which upon turbulence from the plasma jet, transports the melted base material into the melt pool [49]. Due to a high heat sink, rapid solidification occurs, allowing for chemical diffusion between the liquids. Such macrosegregations, known for their high hardness, can act as sites for hydrogen embrittlement.

The exclusive occurrence of type-II boundaries in the CXT sample is linked to the allotropic transformation (ferrite-δ → γ) in the CGHAZ during cooling [50]. The type-II boundary results from the mobile interface between the substrate and coating, projecting into the coating during cooling. Notably, the type-II boundary advances more rapidly in the PGS region than in the CDGS region. Recent studies [16,51] link type-II boundaries to sulfide stress corrosion cracking (SSCC), emphasizing their role in creating a conducive environment for SSCC.

The results of EDS microanalysis at the interface of the STT sample is shown in Fig. 7**(a)**, whereas that of the CXT sample is displayed in Fig. 7**(b)**. In both cases, the EDS elemental mapping reveals the presence of a chemical composition gradient involving Ni, Si, Cr, C, B, and Fe. While Ni and Cr were mostly observed in the coating part of the interfaces, C, and B were observed to be in relatively smaller amounts uniformly distributed over the interfaces. Most importantly, there was an observed heterogeneous distribution of Si and Fe across the interfaces, where their respective amounts decreased with increasing proximity to the interface. This signifies that the chemical composition gradient is not as steep as one may observe in mechanical bonding [52], indicating that the PPTAW process resulted in metallurgical bonding between the coating and the substrate, irrespective of the deposition trajectory used to prepare the samples.

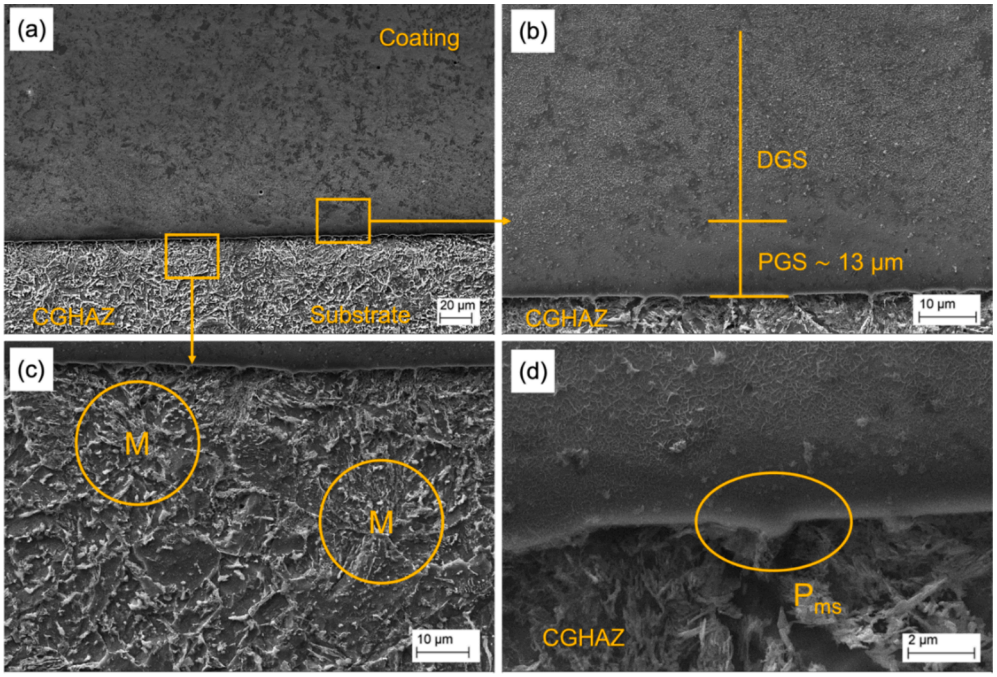

Fig. 5. Interface of sample STT (a) overview of the coating/substrate interface, **(b)** observable zones of planar growth solidification (PGS) and dendritic growth solidification (DGS) at the interface, **(c)** coarse-grained heat-affected-zone (CGHAZ) with martensite laths (M), and **(d)** peninsula-like macrosegregation (P_{ms}) at the interface.

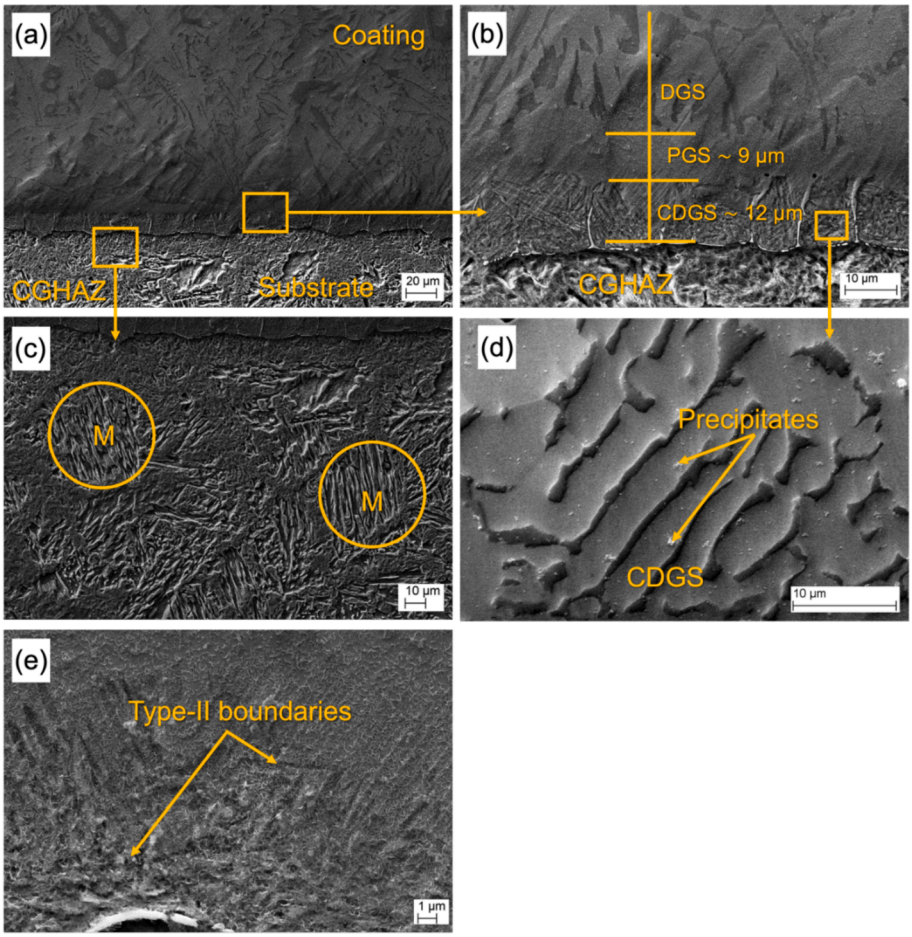

Fig. 6. Interface of sample CXT (a) Overview of the coating/substrate interface, **(b)** observable zones of cellular-dendritic growth solidification (CDGS), planar growth solidification (PGS) and dendritic growth solidification (DGS) at the interface, **(c)** Coarse-grained heat-affected-zone (CGHAZ) with martensite laths (M), **(d)** CDGS containing interdendritic precipitates, and **(e)** Type-II boundaries observed at the interface.

3.2. Thermal analyses

Supplementary Fig. S1**(a)** illustrates the heat simulation of the midpoint of the STT coating, while Fig. S1**(b)** depicts the cross-sectional heat distribution of the STT sample. Notably, two distinct zones of heat evolution are evident, namely the middle zone and the coating/substrate interface transition zone (TZ). Since the STT method proceeded with four passes for coating deposition, thermal analyses considered the first and last passes of the deposited layers individually and unified the second and third passes (mid) since they were centrally located. Similarly, supplementary Fig. S2**(a) and** Fig. S2**(b)** present visualizations of the midpoint of the CXT coating and the corresponding heat distribution in the cross-section of the CXT sample, respectively. The morphology of the cross-section of this sample allowed for thermal analyses in two distinct regions: the center (mid) and the side.

Fig. 8 presents the results of thermal analyses, illustrating the temperature evolution and cooling rates of the examined samples as predicted by FEM simulations. In the case of the STT sample at the coating middle zone (MZ), the last run exhibited the highest recorded temperature (T_{max}) among the passes at 1636 °C (Fig. 8**(a)**), accompanied by a corresponding cooling rate in the range of 1200 – 800 °C ($CR_{1200\text{-}800}$) of 86 K/s. A similar trend was observed at the interface, where the last pass reached a T_{max} of 1408 °C, the highest among the passes (Fig. 8**b)**), with a $CR_{1200\text{-}800}$ of 94 K/s. Notably, both the MZ and the interface indicated higher heat and cooling rates at the coating sides (first and last passes) than a the center (mid pass). The CXT sample yielded contrasting results. At the MZ of this sample, the T_{max} of the mid pass was higher at 1621 °C (Fig. 8**(c)**), with a $CR_{1200\text{-}800}$ of 87 K/s. Similarly, at the interface (Fig. 8 **(d)**), relative to the side pass, the mid pass had a higher T_{max} of 1336 °C and $CR_{1200\text{-}800}$ of 75 K/s. Table 3 provides a summary of the thermal analysis results.

The results reveal that, for both deposition techniques, the heat input was similar. For example, the highest recorded T_{max} for the STT sample was 1636 °C, and for the CXT sample, it was 1621 °C. This similarity can be attributed to the use of the same PTA current of 70 A in both techniques. However, the regions of heat concentration differed. In the STT sample, higher temperature evolution was observed at the sides relative to the center, while in the CXT sample, the opposite was true. Considering that most of the load bearing occurs at the center [53], the temperature evolution at this location is a crucial consideration. In the STT sample, where heat concentration was higher at the coating sides than at the center, the dissipation of heat during the cooling period was faster. This was due to the exothermic dissipation of heat to the surroundings encountering little to no obstacles. In contrast, the CXT sample exhibited greater heat retention, taking a relatively longer time to cool down. The slower exothermic activity in this case resulted from the coating sides acting as temporary thermal barriers to heat dissipation [54]. The level of heat during the PPTAW process directly influences the structure and the evolution of primary and secondary phases in the prepared coatings. Notably, a high heat input during the PPTAW process has been reported to increase the coating-substrate dilution [55], fostering the diffusion of materials from the substrate into the coating and thereby altering the integrity of the coating material. Most importantly, the observed disparities in the heat retention and cooling rates of the investigated

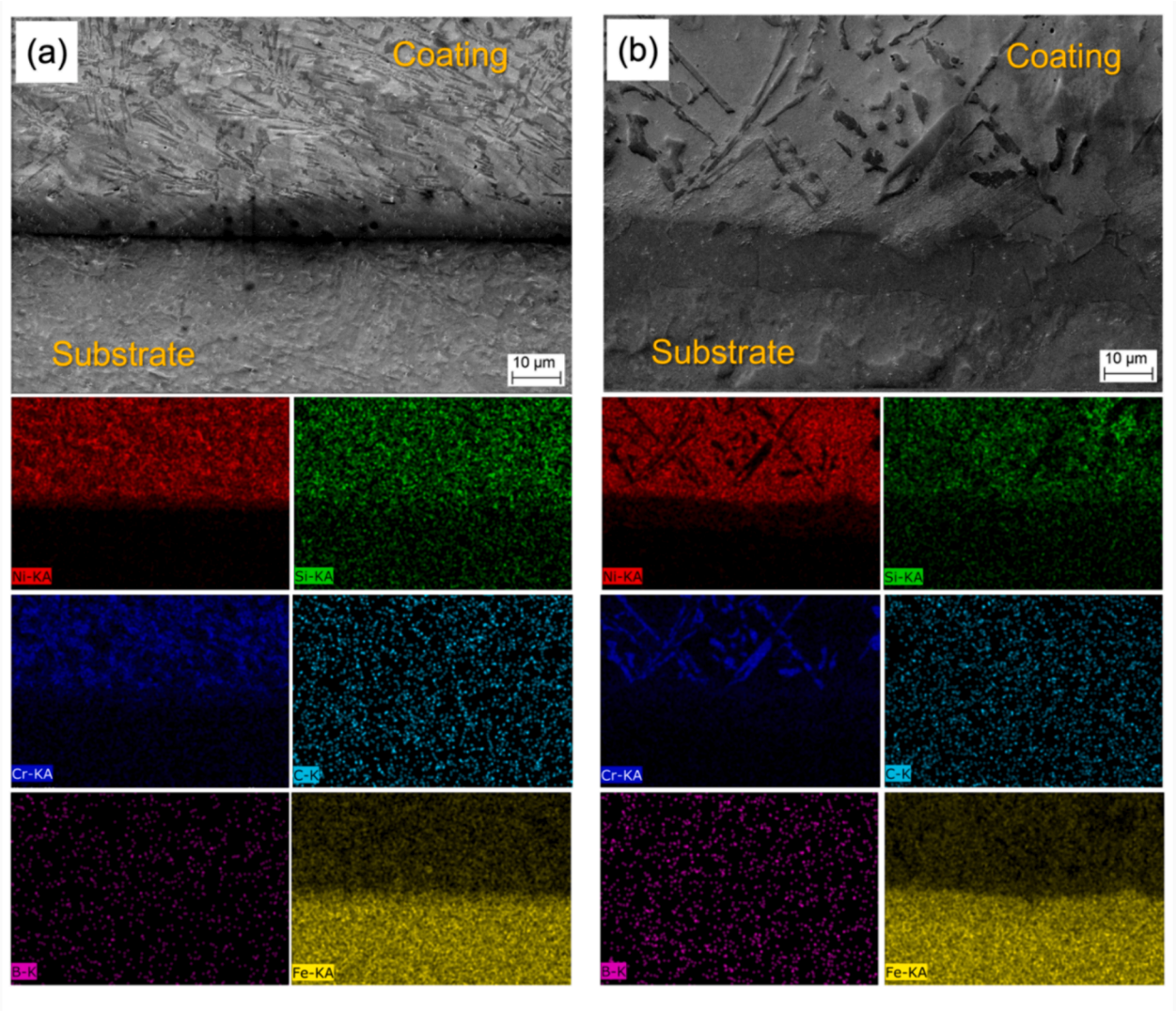

Fig. 7. Chemical composition at the interface (a) SEM image of the interface of sample STT with EDS chemical composition maps and **(b)** SEM image of the interface of sample CXT with EDS chemical composition maps.

samples are a precursor to anticipated resulting microstructural differences.

To corroborate the observation of higher heat retention in the CXT sample over the STT sample from FEM analyses, an experimental determination of the cooling rate was carried out by investigating the dendrite arm spacing (DAS). Fig. 9 displays optical micrographs of the specimens' interfaces with computed DAS at the coating middle zone (MZ). Both samples exhibit a coarse dendritic structure with intergranular non-equilibrium eutectics at the MZ. Notably, the STT sample (Fig. 9**(a)**) displays closely neighbored dendrites, characterized by an average DAS of approximately 11 μm. Conversely, the CXT sample (Fig. 9**(b)**) exhibits a relatively larger spacing, with an average DAS of approximately 16 μm. A closer examination of their respective microstructures was then undertaken using SEM coupled with an EDS system.

Fig. 10 presents SEM images of the MZ for both the STT sample (Fig. 10**(a)**) and the CXT sample (Fig. 10**(b)**). EDS chemical composition mapping reveals a predominant Nickel matrix with dispersed Cr-rich phases. The estimated T_{max} of 1636 °C and 1621 °C for the STT and CXT samples, respectively, are sufficient for complete melting of the Ni-based matrix phase (T_m = 1455 °C) but not for complete dissolution of Cr (T_m = 1907 °C). It is evident that the dispersion of Cr-rich phases in the matrix results from the partial melting of Cr in the completely melted Ni matrix. Additionally, the distinct dendritic structure of the CXT sample, despite its larger DAS, is attributed to its relatively higher heat retention and slower cooling, promoting nucleation of secondary Cr-rich phases during coating solidification. This is in accordance with recent reports by Gu et al. [56] who also found larger DAS corresponding to slower cooling rates. The observation of higher heat retention in the CXT sample from FEM further corroborates this observation. Thermal distribution and heat input during PPTAW coating deposition has been reported to directly influence the evolution of grains and strengthening phases [57], which alter the resulting properties of the deposited coatings. In this regard, investigations into phase evolution and grain refinement were undertaken using XRD and EBSD respectively.

3.3. Phase and grain size evolution

The diffraction patterns from XRD analyses, illustrated in Fig. 11, provide an examination of the deposited powder, STT coating, and CXT coating. Peak identification was achieved by correlating them with the Inorganic Crystal Structure Database (ICSD). The discerned phases include γ-Ni (ICSD No. 260169) possessing a face-centered cubic (FCC) structure (a = b = c = 3.528 Å), $Cr_{23}C_6$ (ICSD No. 617488) with an FCC structure (a = b = c = 10.630 Å), $Ni_{31}Si_{12}$ (ICSD No. 9106) exhibiting a hexagonal structure (a = b = 6.671 Å, c = 12.288 Å), Cr_3C_2 (ICSD No. 181711) with an orthorhombic structure (a = 5.485 Å, b = 2.789 Å, c =

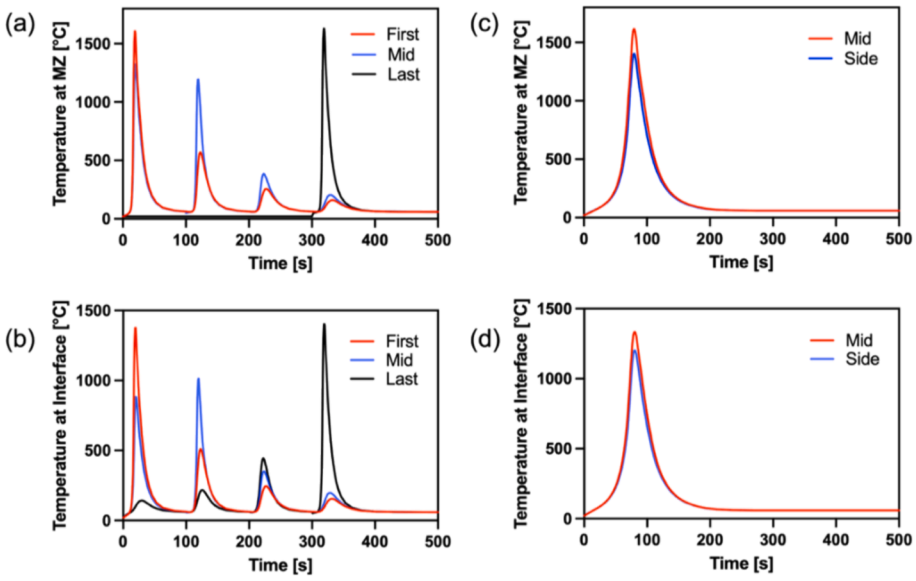

Fig. 8. Visualization of registered PPTAW heat input at the middle zone (MZ) and interface during sample preparation (a) MZ of sample STT, **(b)** interface of sample STT **(c)** MZ of sample CXT, and **(d)** interface of sample CXT.

Table 3
Results of numerical thermal analyses.

STT	First pass MZ T_{max} [°C]	1615.31
	First pass MZ $CR_{1200\text{-}800}$ [K/s]	75.78
	Mid pass MZ T_{max} [°C]	1328.17
	Mid pass MZ $CR_{1200\text{-}800}$ [K/s]	76.21
	Last pass MZ T_{max} [°C]	1636.12
	Last pass MZ $CR_{1200\text{-}800}$ [K/s]	86.81
	First pass interface T_{max} [°C]	1381.48
	First pass interface $CR_{1200\text{-}800}$ [K/s]	84.44
	Mid pass interface T_{max} [°C]	1018.59
	Mid pass interface $CR_{1200\text{-}800}$ [K/s]	NR*
	Last pass interface T_{max} [°C]	1408.76
	Last pass interface $CR_{1200\text{-}800}$ [K/s]	93.88
CXT	Mid MZ T_{max} [°C]	1621.06
	Mid MZ $CR_{1200\text{-}800}$ [K/s]	87.25
	Side MZ T_{max} [°C]	1407.16
	Side MZ $CR_{1200\text{-}800}$ [K/s]	84.40
	Mid interface T_{max} [°C]	1336.06
	Mid interface $CR_{1200\text{-}800}$ [K/s]	75.24
	Side interface T_{max} [°C]	1203.14
	Side interface $CR_{1200\text{-}800}$ [K/s]	73.98

* NR – value not recorded in the specified temperature range.

11.474 Å), and Ni_3B (ICSD No. 75794) characterized by an orthorhombic structure (a = 5.232 Å, b = 6.609 Å, c = 4.389 Å). Notably, at 2θ ~ 52°, the prominence of the (1 1 1) γ-Ni phase was evident in the powder, with a sustained high intensity observed in the STT coating. However, this intensity diminished in the CXT coating. Concurrently, at this angle, minor quantities of (0 0 6) $Ni_{31}Si_{12}$ and (1 0 2) Ni_3B were observed to overlap with the γ-Ni phase. Similarly, at 2θ ~ 61°, the (0 0 2) γ-Ni phase overlapped with the (0 0 6) $Cr_{23}C_6$ phase in both the powder and the coatings. Notably, the CXT coating exhibited a higher intensity of the $Cr_{23}C_6$ phase in relation to the γ-Ni phase, which retained a higher intensity in the powder and STT coating. Furthermore, at 2θ ~ 92°, the powder displayed a prominent intensity of the (0 2 2) γ-Ni phase, whereas after coating deposition, the STT coating manifested an overlap of this phase with the (0 6 6) $Cr_{23}C_6$ phase. A similar overlap was observed in the CXT coating, albeit with significantly reduced intensity relative to the STT coating. Additionally, the CXT coating uniquely exhibited a prominent peak corresponding to the (1 0 4) Cr3C2 phase at 2θ ~ 41°. The (2 1 3) Cr_3C_2 phase overlapped with the (0 0 6) $Cr_{23}C_6$ phase at 2θ ~ 62°.

Although the predominant peaks corresponded to the γ-Ni, Cr_3C_2, and $Cr_{23}C_6$ phases, XRD identified relatively lower intensities of the $Ni_{31}Si_{12}$ phase at 2θ ~ 49°, 52°, 55°, and 80°, and the Ni_3B phase at 2θ ~ 44°, 52°, 54°, and 66°. These phases were more pronounced in the powder than in the STT and CXT coatings. Similar observations have been reported by Deenadayalan et al. [58] and Chen et al. [59] upon deposition of NiCrBSi coatings using PTAW technology. The analysis reveals that the most prominent phase in the coatings was the γ-Ni phase, owing to its higher composition. However, the higher heat retention in the CXT coating facilitated the formation and precipitation of chromium carbides, evident from the elevated intensities of the $Cr_{23}C_6$ and Cr_3C_2 phases in this coating relative to the STT coating. Nevertheless, the STT coating exhibited a pattern comparable to the powder, indicating its superior ability to preserve the integrity of the coating material upon solidification. To delve further into the grain refinement and evolution of grain boundaries in the coatings, EBSD analysis was carried out.

Fig. 12 presents the results from EBSD analysis, which reveal equiaxed grains with different crystallographic orientations. The unit triangle indicates [1 1 1], [1 0 1], and [0 0 1] orientations, which correspond to the face-centered cubic (FCC) structure of the Nickel (γ-Ni) and $Cr_{23}C_6$ phases. The unit quarter displays [0 1 0], [1 0 0], and [0 0 1] orientations, which represent the orthorhombic structure of the Cr_3C_2 phase. In all, three phases (γ-Ni, $Cr_{23}C_6$, and Cr_3C_2) were identified from the EBSD analysis. The most significant reason for this observation is that the concentrations of the nickel silicide ($Ni_{31}Si_{12}$) and trinickel boride (Ni_3B) phases might be too low in the coatings, thereby falling under the detection limit of EBSD. This also further corroborates the dominance of the γ-Ni, $Cr_{23}C_6$, and Cr_3C_2 phases in the coatings, as observed from XRD analysis.

The inverse pole figure (IPF) map of the coating produced by the STT method is shown in Fig. 12**(a)**. The grain boundaries were classified according to their misorientation angles: high angle grain boundaries (HAGBs) with misorientation angles greater than 15° are shown in black, low angle grain boundaries (LAGBs) with misorientation angles between 5° and 15° are shown in red, and LAGBs with misorientation angles between 2° and 5° are shown in white [60]. The grain size distribution for the STT coating, considering all phases, is shown in Fig. 12 **(b)**. The average grain size was estimated to be about 17.4 μm (Grain tolerance angle, GTA = 2°). Individually, the γ-Ni phase had an average grain size of 16.4 μm (GTA = 2°). The $Cr_{23}C_6$ phase exhibited an average

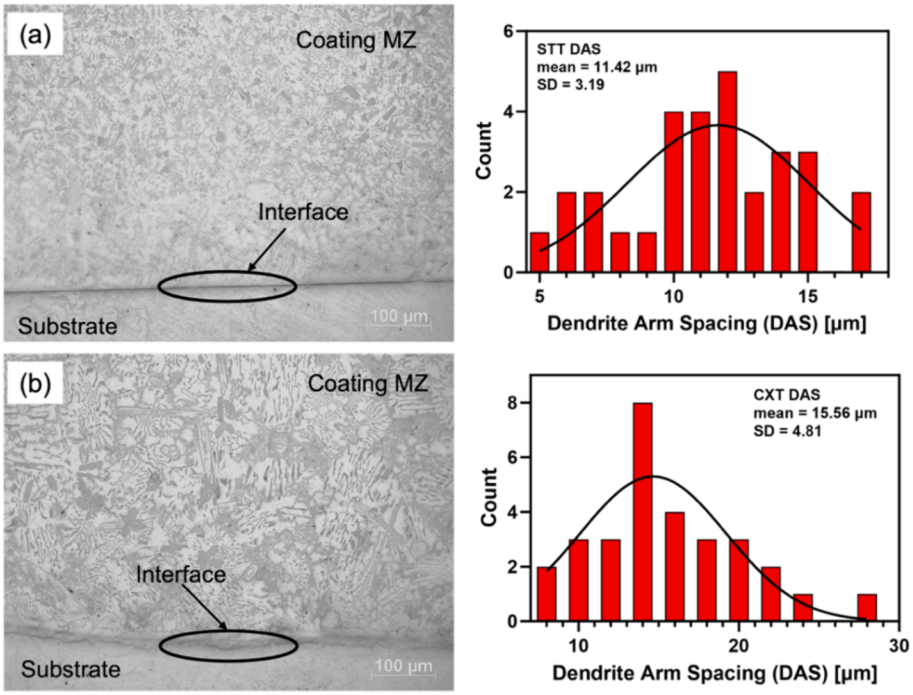

Fig. 9. Optical micrographs of the microstructure of the MZ of the investigated samples with accompanying dendrite arm spacing (DAS) **(a)** STT sample and **(b)** CXT sample.

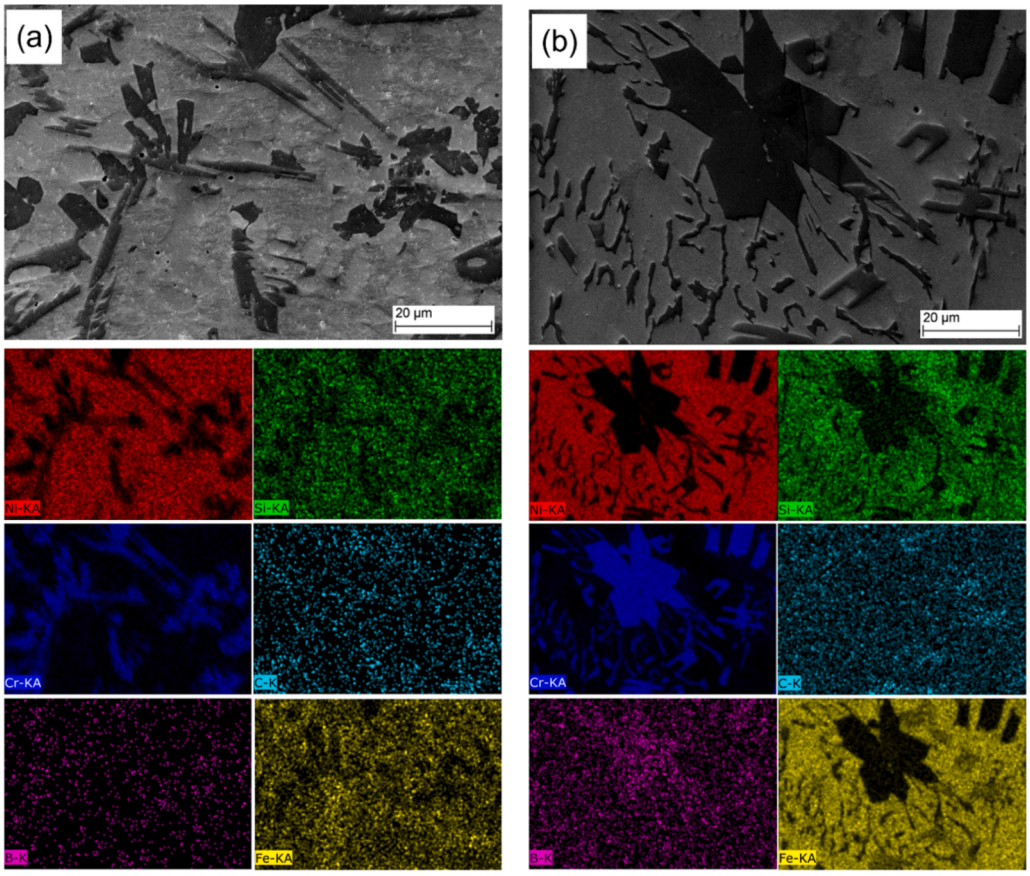

Fig. 10. SEM images and EDS chemical composition of maps of investigated samples **(a)** microstructure of the MZ of STT and **(b)** microstructure of the MZ of CXT.

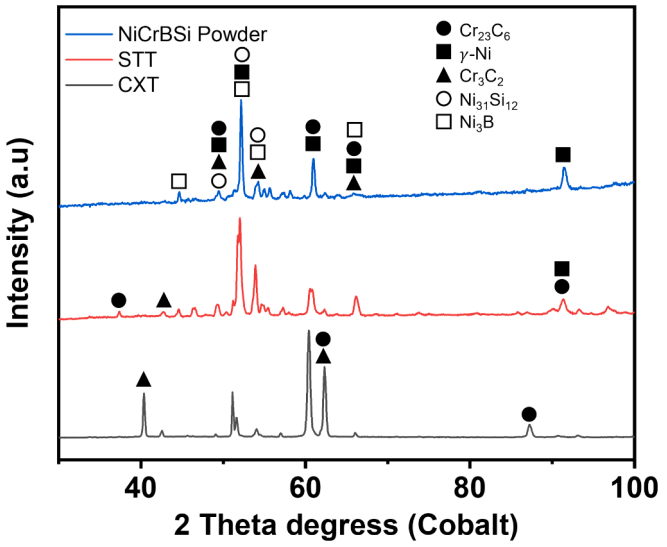

Fig. 11. X-ray diffraction patterns of the NiCrBSi powder, STT coating and CXT coating.

grain size of 14.6 μm (GTA = 2°), and the Cr_3C_2 phase had an average grain size of 8.2 μm (GTA = 2°). Fig. 12**(c)** displays the EBSD phase map of the STT coating, which reveals the spatial distribution of the detected phases. The phases are color-coded as follows: blue for the γ-Ni phase, green for the $Cr_{23}C_6$ phase, and red for the Cr_3C_2 phase. The phase quantification indicates that the γ-Ni phase constitutes about 73 % of the analyzed area, while the $Cr_{23}C_6$ and Cr_3C_2 phases account for about 26 % and 1 %, respectively.

The IPF map of the CXT coating is shown in Fig. 12**(d)**, which exhibits the same three phases as the STT coating. However, the grain size map (Fig. 12**(e)**) gives an average grain size of 68.7 m (GTA = 2) for all phases combined, which is about 4 times larger than the average grain size measured for the STT coating. The individual phases have average grain sizes of 69.6, 8.4, and 6.6 μm (GTA = 2°) for the γ-Ni, $Cr_{23}C_6$, and Cr_3C_2 phases, respectively. The EBSD phase map of the CXT coating is depicted in Fig. 12**(f)**. The phase composition follows a similar trend as the STT coating, with the γ-Ni phase being the most dominant at about 81 %, followed by the $Cr_{23}C_6$ phase at about 18 %, and the Cr_3C_2 phase having the lowest fraction of less than 1 %.

The average grain size and the fractions of HAGBs and LAGBs for the γ-Ni phase in both STT and CXT coatings are summarized in Fig. 12**(g)**. The number fractions of each type of grain boundary for this phase are given in supplementary **Figure S3**. The STT coating exhibited a higher fraction of HAGBs (about 66 %) than LAGBs (about 34 %), while the CXT coating showed a dominant fraction of HAGBs (about 74 %) compared to LAGBs (about 26 %). Fig. 12**(h)** shows a similar comparison for the $Cr_{23}C_6$ phase, with the number fractions of grain boundaries provided in supplementary **Figure S4**. The STT coating had a larger fraction of LAGBs (about 72 %) than HAGBs (about 28 %) for this phase, whereas the CXT coating had an opposite trend, with a higher fraction of HAGBs (about 72 %) than LAGBs (about 28 %). For the Cr_3C_2 phase, both coatings had a predominant fraction of HAGBs, as depicted in Fig. 12**(i)**. The STT coating and the CXT coating had HAGBs of about 56 % and 66 %, respectively, and LAGBs of about 44 % and 34 %, respectively. Supplementary **Figure S5** shows the detailed number fractions of the grain boundaries for this phase for both samples.

The results show that the γ-Ni phase in both samples exhibits higher interfacial energy, as evidenced by the greater presence of HAGBs, thereby enhancing the coatings' stability by increasing their ability to effectively impede the motion of dislocations [61]. In essence, the γ-Ni phase contributes significantly to the strength of the coatings. However, the $Cr_{23}C_6$ phase in the STT coating is observed to be slightly unstable, owing to its greater proportion of LAGBs [62]. The results indicate that the CXT approach is effective in producing coatings with stable strengthening phases, relative to the STT approach. Nevertheless, given the superior stability of the primary γ-Ni phase in both coatings, the performance of the coatings will not depend on the stability of the other strengthening phases, but rather on contributing conditions such as the morphology of the grains, the extent of grain refinement, and the concentration of strengthening phases. [63]. The study reveals that the STT coating possessed significantly smaller grains relative to the CXT coating. According to the literature, smaller grains are often associated with better mechanical properties [64–67]. Some studies have even reported a direct relationship between grain refinement and improved corrosion resistance and wear resistance [68–70].

3.4. Corrosion resistance

The E_{ocp} curves recorded over time for the coatings prepared by the STT and CXT methods are depicted in Fig. 13**a**. The initial E_{ocp} values were high for both samples at −415 mV vs. Ag/AgCl and −380 mV vs. Ag/AgCl for the STT and CXT samples respectively. However, they started to fall sharply from t = 1 s until the curve stabilized after approximately 250 s for the STT sample to −458 mV vs. Ag/AgCl and after approximately 490 s for the CXT sample to −446 mV vs. Ag/AgCl. Such rapid shifts in E_{ocp} values suggest changes in cathodic or anodic activity rates. In aqueous environments, oxide film formation on the material surface often occurs, leading to unstable electrochemical activity and abrupt fluctuations in E_{ocp} readings. After 250 s, the STT coating exhibited minimal changes in the E_{ocp} over time with a mean E_{ocp} of −495 mV vs. Ag/AgCl. The average E_{ocp} for the CXT sample was −466 mV vs. Ag/AgCl.

The corrosion potential (E_{corr}) is depicted in the Tafel plots in Fig. 13**b** for both samples. The STT sample exhibited an E_{corr} of −468 mV, whereas the CXT sample showed a lower E_{corr} of −487 mV. The corrosion current density (i_{corr}) for the STT sample was lower at 12.8 μA/cm^2 than the CXT sample, which had an i_{corr} of 34.3 μA/cm^2. This disparity underscores a noteworthy enhancement in the corrosion resistance of the STT coating relative to the coating produced through the CXT method.

At a temperature of approximately 301 K, the electrochemical impedance measurements were evident following a 300-second potential stabilization. Nyquist plots (Fig. 13**c**) were then generated. The plots are characterized by the typical Nyquist semi-circles as seen in reported studies on the corrosion resistance of Ni-based coatings [71,72]. Most importantly, singular semi-circular loops are observed for both samples in the Nyquist domain corresponding to high frequencies. This phenomenon can be attributed to the resistance to charge transfer occurring in the investigated specimens. A fitted equivalent electrical circuit, depicted in Fig. 13 **(c)** inset, was used to represent the corrosion system based on impedance curves. This equivalent circuit (EC) comprises a series-connected R-C group, a constant phase element (CPE), and two resistors. In this proposed EC, the solution's resistance is denoted as R_s, while R_1 denotes the charge transfer resistance (R_{ct}), and CPE_1 is the passive film capacitance. The resulting Nyquist plots in Fig. 13 (c) illustrate a larger diameter for the STT coating signifying relatively better corrosion resistance over the CXT coating. Additionally, the R_{ct}, indicative of corrosion polarization resistance, was marginally higher for the STT coating at 2550 Ω • cm^2, whereas the CXT coating exhibited an R_{ct} value of 2500 Ω • cm^2. These findings align with the Tafel analysis, which also indicated superior corrosion resistance for the STT coating. Likewise, the Bode spectra of the samples, as depicted in Fig. 13**d**, elucidate the frequency response of the specimens up to 100 kHz. Analysis of the curves reveals that the STT sample displays the highest impedance, correlating with enhanced corrosion resistance. Fig. 13**e** reveals a notable observation: the CXT specimen exhibits a comparatively higher phase shift angle within the identical frequency response range when compared to the STT specimen. This observation

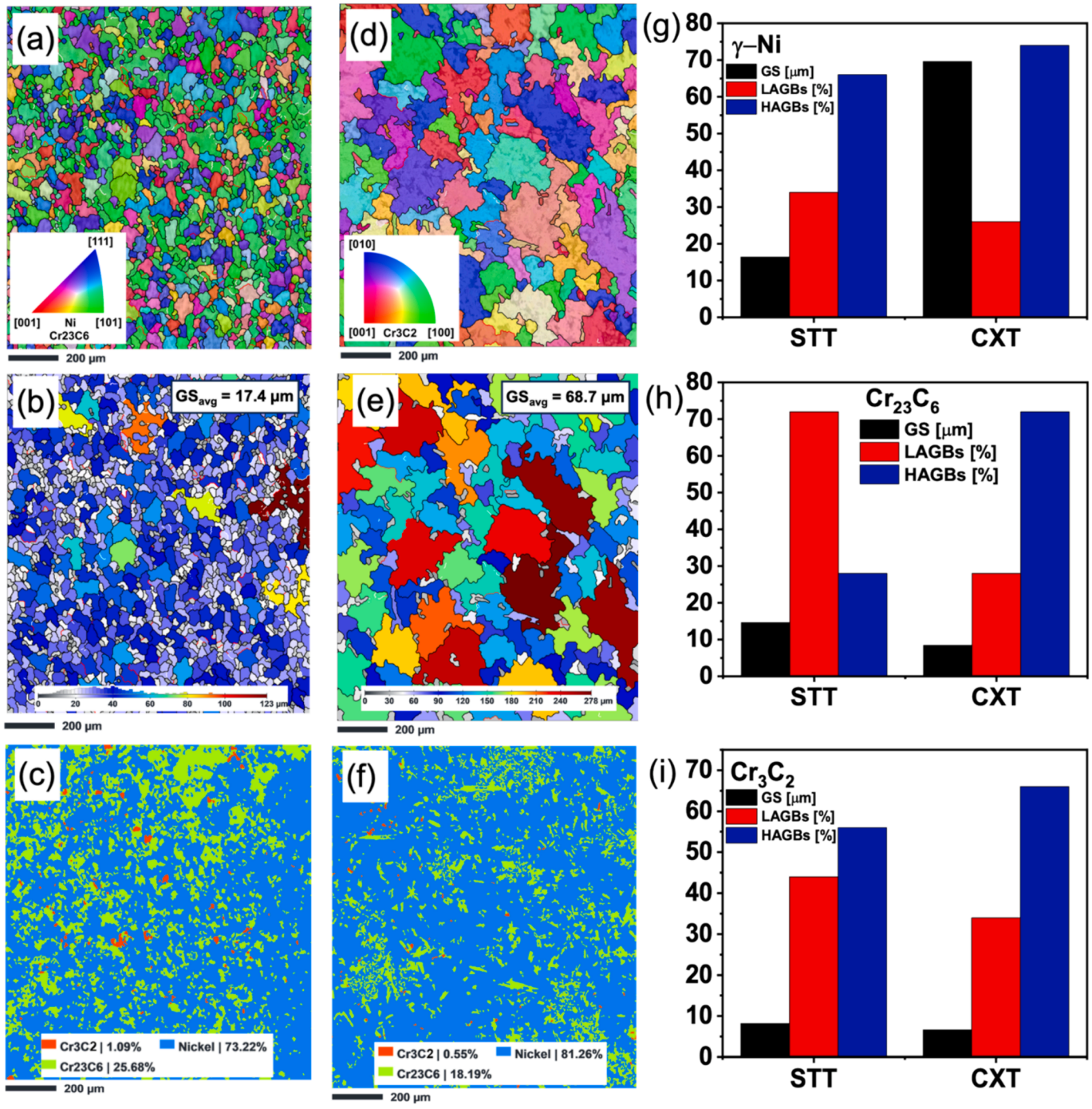

Fig. 12. Electron backscatter diffraction (EBSD) characterization results (a) IPF map of STT coating, **(b)** Grain size map of STT coating **(c)** EBSD phase composition map of STT coating **(d)** IPF map of CXT coating, **(e)** Grain size map of CXT coating, **(f)** EBSD phase composition map of CXT coating **(g)** Comparison of grain size, LAGBs and HAGBs in the γ-Ni phase **(h)** Comparison of grain size, LAGBs and HAGBs in the $Cr_{23}C_6$ phase, and **(i)** Comparison of grain size, LAGBs and HAGBs in the Cr_3C_2 phase.

suggests superior surface conditions of the CXT specimen during the EIS non-destructive test. However, despite this advantage, the overall corrosion resistance of the CXT specimen was found to be lower than that of the STT specimen, as indicated by the results of the Tafel and Nyquist analyses. Table 4 presents a summary of the corrosion parameters.

The heightened corrosion resistance observed in the STT sample relative to the CXT sample can be ascribed, in part, to the higher concentration of the $Cr_{23}C_6$ phase in the former (25.56 %) as opposed to the latter (18.19 %). The corrosion tendencies of the $Cr_{23}C_6$ phase are linked to the formation of a passivating layer, Cr_2O_3, within the material. This phenomenon arises from volumetric changes resulting from changes in Gibbs free energy. The compound is formed through the reaction in **Eq. (4)**.

$$4/93Cr_{23}C_6(s) + O_2(g) \rightleftharpoons 46/93Cr_2O_3 + 8/31 + CO_2(g) \quad (4)$$

Evidently, there is transformation of chemical composition from being C-rich to O-rich as the reaction proceeds to the left. To further understand the rapid oxidation of $Cr_{23}C_6$, it is necessary to consider the standard enthalpy of formation (ΔH_f). Notably, the ΔH_f for Cr_2O_3

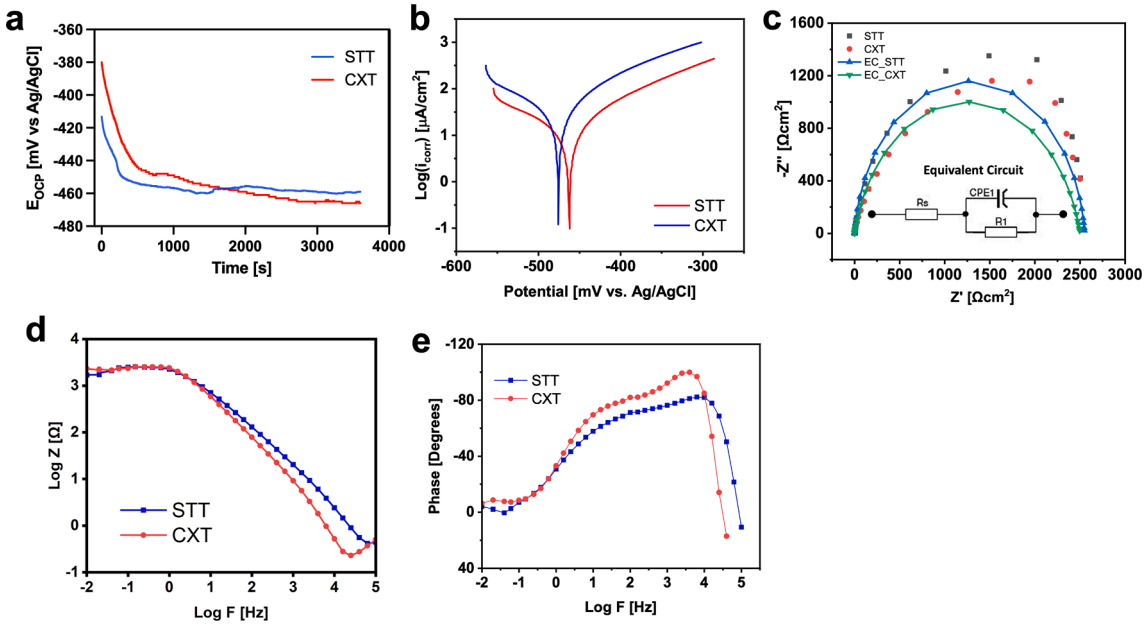

Fig. 13. Corrosion resistance results a. Open circuit potential (E_{ocp}) curves, **b.** Tafel plots, **c.** Nyquist impedance plots with fitted equivalent circuit curves, **d.** Impedance spectra as a function of frequency, **e.** Bode phase shift plots.

Table 4
Summary of corrosion resistance parameters.

Sample	E_{ocp}	i_{corr}	E_{corr}	R_s	CPE_1	n	R_{ct}
	mV vs. Ag/AgCl	μA/cm²	[mV]	Ω • cm²	x10⁻⁶F • S^(n-1) • cm⁻²	–	Ω • cm²
STT	−495	12.8	−468	1.0	45.3	0.94	2550
CXT	−466	34.3	−487	1.0	36.7	0.86	2500

(−612.8 kJ/mol) is comparatively lower than that of $Cr_{23}C_6$ (−285.8 kJ/mol). Consequently, under the same conditions, Cr_2O_3 attains greater stability, fostering spontaneous reactions. Corroborative evidence from Rashid et al. [73] and Wu et al. [74] concerning the oxidation of alloys containing $Cr_{23}C_6$ aligns with these findings.

The examination of corrosion immersion morphologies was conducted using SEM, as illustrated in Fig. 14. In the case of the STT morphology (Fig. 14**(a)**), the predominant form of corrosion manifested

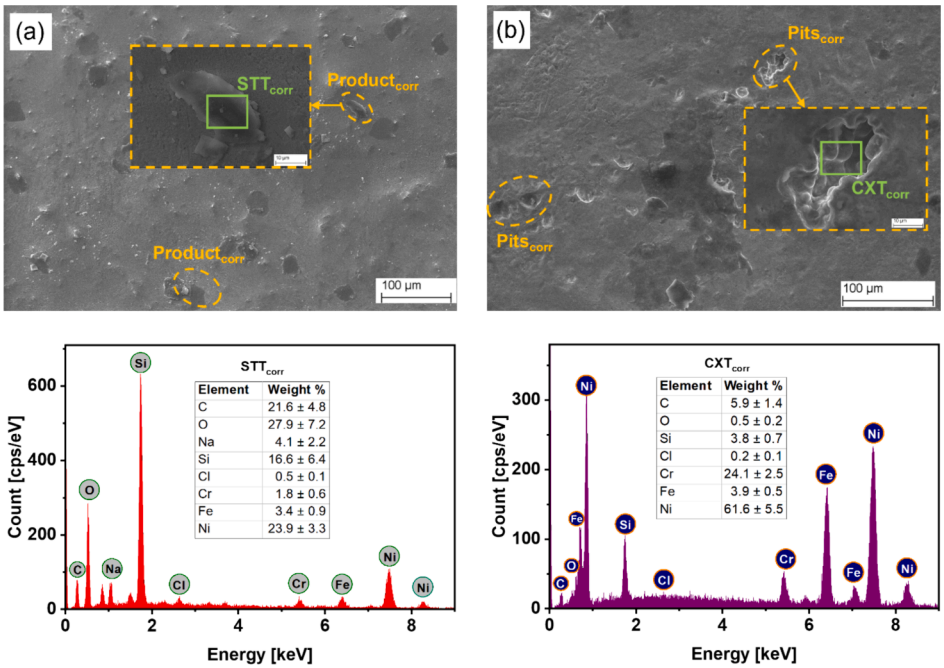

Fig. 14. (a) Corrosion morphology of sample STT showing the structure and chemical composition of corrosion products and **(b)** Corrosion morphology of sample CXT showing the structure and chemical composition of corrosion pits.

as the development of corrosion products on the surface. The elemental composition of these products, analyzed through EDS, indicated a significant presence of carbon (C) and oxygen (O), implying the early formation of an oxide passivating layer as corrosion progressed within the specimen [74]. In addition to the coating material's chemical composition, the corrosion products exhibited traces of sodium (Na) and chlorine (Cl). This can be attributed to the 3.5 % NaCl solution used for corrosion testing. In contrast, the corrosion morphology of the CXT sample (Fig. 14**(b)**) revealed pitting corrosion as the primary mode. EDS analysis of the pits in the CXT morphology also revealed the presence of C and O, like the observations in the SST morphology. Notably, The EDS results indicate a high concentration of chromium (Cr) in the pits of the CXT corrosion supporting the role of Cr_2O_3, as indicated in **Eq.** (4), in the formation of corrosion pits in this specimen.

Fig. 15 displays backscattered electron (BSE) images along with corresponding EDS elemental maps, elucidating the immersion morphologies of the samples. The BSE images identify two distinct regions: flattened black and grey areas. In the case of the STT specimen (Fig. 15 **(a)**), the black regions correspond to the corrosion products formed on the surface. The elemental maps reveal a predominant presence of Cl and Na in these products, accompanied by a high concentrations of Cr. Conversely, the Fe and Ni contents are diminished, indicating potential selective corrosion of the STT coating, possibly influenced by the participation of unmelted particles, as noted by Somervuori et al. [75].

Observations from the CXT immersion morphology (Fig. 15**(b)**), show the flattened black regions observed in the BSE images correspond to the corrosion pits identified in Fig. 15**(b)**. Notably, EDS mappings highlight elevated contents of Cr and O in these pits. In the context of face-centered cubic (FCC) systems like Ni-based coatings, specific crystallographic planes, particularly {1 1 1}, demonstrate dense packing and inherent resistance to corrosion. This resistance decreases in the order of {1 1 1}, {1 0 0}, and {1 1 0} planes [76]. From XRD analysis, the peak corresponding to the {1 1 1} Nickel phase is more prominent in the STT coating than in the CXT coating. This observation provides evidence supporting the STT coating's reduced susceptibility to pitting corrosion.

3.5. Hardness

Vickers microhardness measurements were conducted to assess the extent to which the different coating deposition techniques affects the hardness of the resulting products. Measurements were taken at room temperature along the cross-section of each sample from the coating through the substrate material. Three regions of hardness were identified upon measurement. These are the coating, heat-affected zone (HAZ)

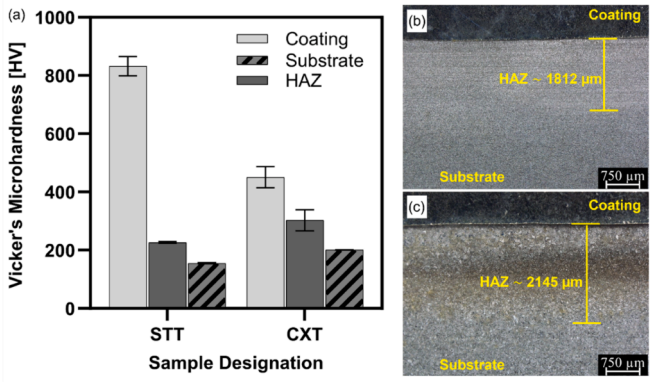

Fig. 16. (a) Vicker's microhardness of the cross-section of investigated samples, **(b)** digital micrograph of STT, and **(c)** digital micrograph of CXT.

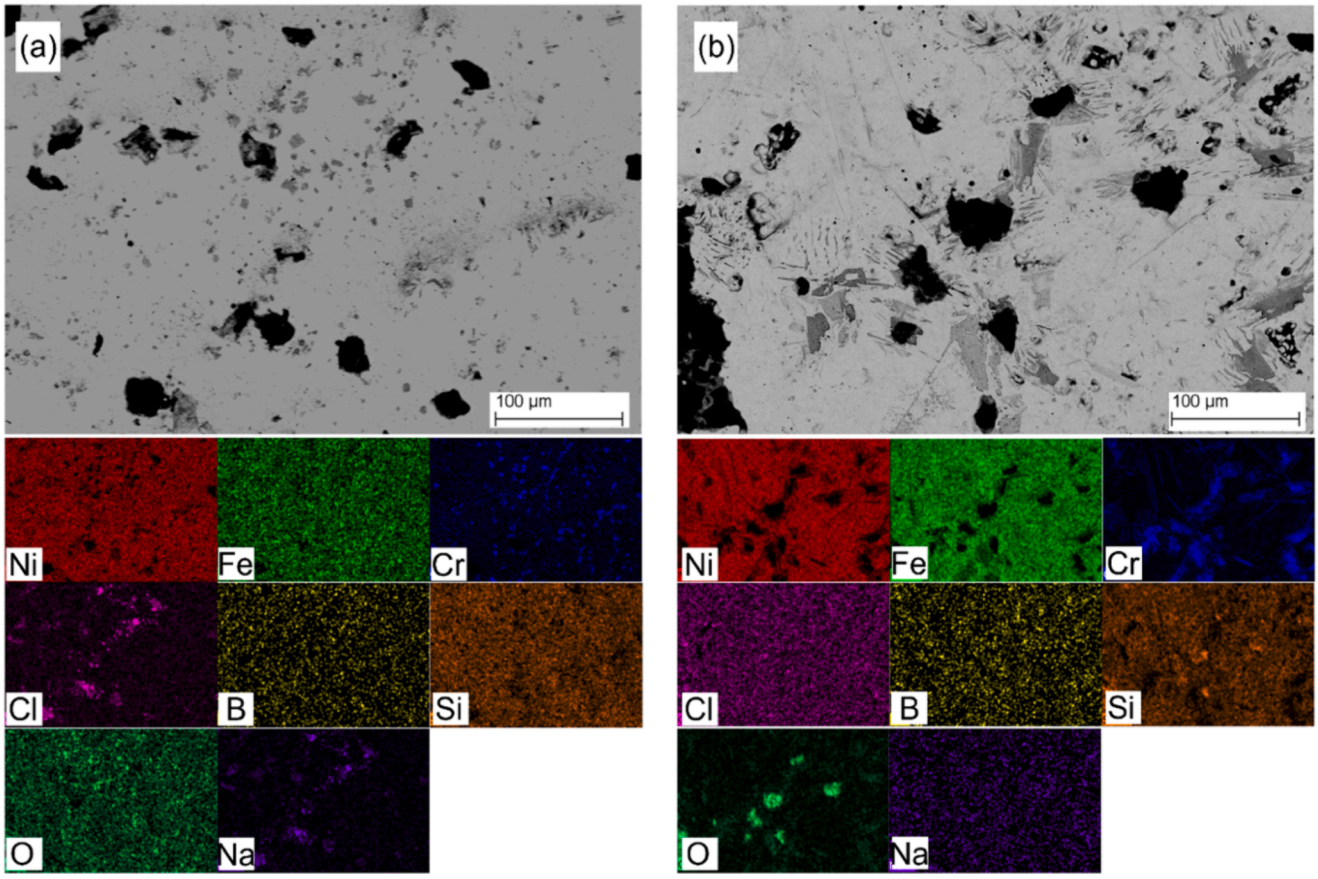

Fig. 15. Backscatter electron (BSE) images of corrosion morphology with EDS chemical composition maps of corrosion products **(a)** sample STT **(b)** sample CXT.

and the substrate. The results of the microhardness measurements are presented in Fig. 16**(a)** for both samples. It is observed in both samples that the hardness was highest in the coating, followed by the HAZ and the substrate measured the least. The coating of the STT sample had a microhardness of 832 Â ± 33 $HV_{1.0}$. The microhardness of the HAZ was estimated to be 226 Â ± 3 $HV_{1.0}$, and that of the substrate measured 155 Â ± 2 $HV_{1.0}$, equivalent to the microhardness of the substrate material before the PPTAW process (Fig. 4**E**). The microhardness of the CXT coating measured 450 Â ± 36 $HV_{1.0}$, showing a decrease of around 50 % compared to the STT coating. In this sample, the HAZ exhibited a microhardness of 302 Â ± 36 $HV_{1.0}$, while the substrate had a microhardness of 201 Â ± 0.2 $HV_{1.0}$.

The results substantiate the superiority of the STT technique in enhancing the hardness of the prepared coatings as well as preserving the integrity of the substrate material, over the CXT technique. The difference in the hardness of the coatings prepared by the two methods can be explained by the difference in grain sizes resulting from these methods. As postulated by the Hall-Petch theory [77], materials with smaller grains have a relatively higher number of grain boundaries, which actively impede dislocation motion, invariably enhancing the strength of the material. From the observed grain refinement induced by the STT approach, this theory holds true for the superior hardness in this coating, over the CXT approach. In Fig. 16**(b)** the cross-section of the STT sample shows a HAZ of approximately 1812 μm, whereas the CXT method resulted in a HAZ of approximately 2145 μm (Fig. 16**(c)**). The most significant reason for this observation is the higher heat retention in the CXT sample as revealed by thermal analyses, causing the substrate to absorb more heat from the coating, therefore enlarging the HAZ. For structural and industrial applications, coatings with smaller HAZs are preferred over the others. This is primarily because, the higher hardness at the HAZs create an environment conducive for the onset of hydrogen embrittlement, eventually reducing the strength and stability of the resulting coating [78].

3.6. Wear resistance

In Fig. 17**(a)**, the progression of the coefficient of friction for coatings

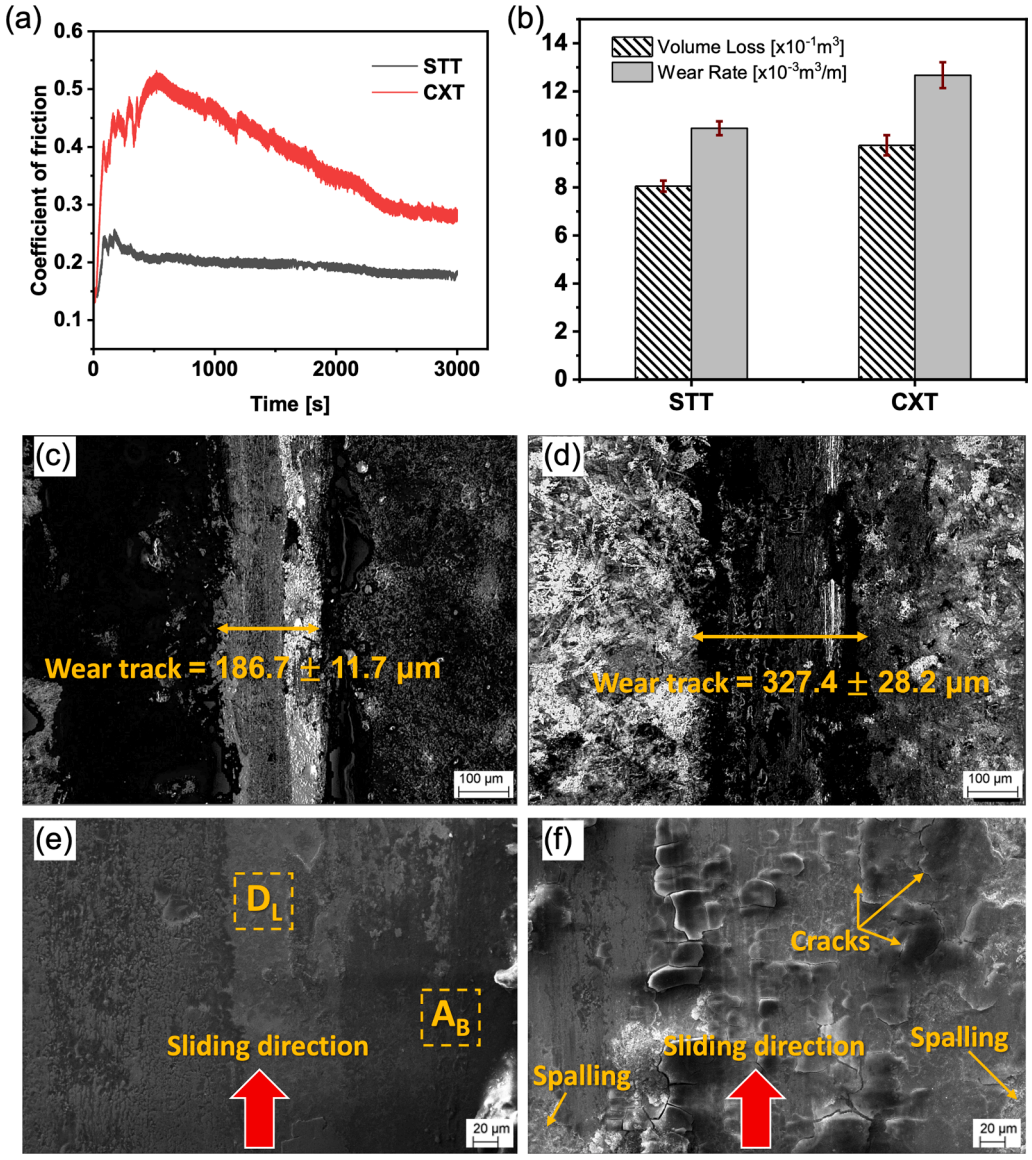

Fig. 17. Tribological properties (a) evolution of coefficient of friction (COF) as a function of time **(b)** volume loss and wear rate **(c)** stereoscopic image of the surface of sample STT after wear test showing the size of the wear track, **(d)** stereoscopic image of the surface of sample CXT after wear test showing the size of the wear track, **(e)** SEM image of the wear track of sample STT showing regions of delamination wear (D_L) and abrasive grooves (A_B), and **(f)** SEM image of the wear track of sample CXT showing the fatigue wear zones characterized by cracking and spalling.

produced through the STT (black) and CXT (red) methods is illustrated. Until the curves begun to exhibit steady state progression after approximately 2500 s, noticeable fluctuations were evident in the COF curves, particularly pronounced in the CXT coating as opposed to the STT coating. These fluctuations signify structural inhomogeneity, primarily attributed to incomplete powder particle melting during the coating process. Despite the observed fluctuations, both samples exhibit a consistent initial reduction in COF. This phenomenon is ascribed to the focal interaction between the test and counter samples, leading to increased compressive pressures and consequent elevated shear stress. The surface in contact undergoes a stepwise process of deformation and fragmentation, thereby expediting the wear process [79]. Notably, the STT technique yields a coating with the lowest COF of 0.19 ± 0.01, while the CXT sample exhibits a COF estimated at 0.29 ± 0.01. An investigation into the volume loss and wear rates of the samples was imperative to gain a better understanding of the disparities in the wear resistance of coatings produced by both techniques.

To calculate the wear rate, Q (m^3/m), **Eq. (5)** was used, where the sliding distance is represented by L_s (m) and the volume loss, by V_s (m^3).

$$Q = \frac{V_s}{L_s} \tag{5}$$

Archard's law states that the volume loss has an inverse proportionality to the hardness. This is law is expressed in **Eq. (6)** [80].

$$V_s = \frac{kWL_s}{H} \tag{6}$$

Where W is the load, k is the wear coefficient and H is the hardness. The computed V_s and Q are graphically presented in Fig. 17**(b)** for both STT and CXT samples. The STT sample exhibited significantly higher wear resistance with a wear rate of $Q = 10.46 \pm 0.29 \times 10^{-3}$ m^3/m. The CXT sample had a wear rate of $Q = 12.67 \pm 0.54 \times 10^{-3}$ m^3/m, about 21.12 % higher than the wear rate of the STT sample. The grain refinement associated with the STT method is a major contributing factor in enhancing the wear resistance of the resultant coating, underscoring the relevance of smaller grains in enhancing the mechanical properties of materials. A corroborative study by [81], reported a direct relationship between grain refinement and improved wear resistance in plasma sprayed NiCrBSi-WC/Co coatings.

The wear mechanisms were investigated using a combination of stereoscopic microscopy and scanning electron microscopy. Fig. 17**(c)** displays the stereoscopic micrograph of the STT sample post wear testing, while Fig. 17**(d)** portrays the equivalent for the CXT sample. Evidently, the counter sample in the wear test generated a more extensive wear track in the CXT coating (approximately 327.4 Â± 28.2 µm) than in the STT coating (approximately 186.7 Â± 11.7 µm). Upon closer examination of the wear track of the STT coating, Fig. 17**(e)** reveals two distinct regions: the delamination wear region (D_L) and abrasive wear grooves (A_B). The D_L region displays prominent ploughing grooves, contributing to the delamination of the material. Notably, both D_L and A_B areas in the STT coating exhibit comparable observable volumes. However, a discernible disparity in wear mechanisms is evident in the CXT coating. While similar D_L and A_B wear areas are observed in the wear track of this coating, additional regions depicting fatigue wear (Fig. 17**(f)**) are present, which were absent in the STT coating's wear track. The fatigue wear regions are characterized by several crack sites displaying branching patterns and propagating within the wear track. Furthermore, the phenomenon of spalling is observed, resulting from the detachment of small material fragments in the wear track due to fatigue cracks. A summary of the tribological properties of the tested samples is presented in Table 5.

Table 5
Summary of tribological properties.

Sample ID	Hardness [HV]	COF	Wear Rate [x$10^{-3}$$m^3$/m]
STT	832.13 Â± 32.98	0.19 Â± 0.01	10.46 Â± 0.29
CXT	450.72 Â± 36.06	0.29 Â± 0.01	12.67 Â± 0.54

COF – coefficient of friction

4. Conclusions

This study delved into the impact of PPTAW directed energy deposition trajectories on the microstructure and performance of additively manufactured single-layered coatings. The investigations focused on two deposition trajectories – straight trajectory (STT) and complex trajectory (CXT) – used to deposit NiCrBSi powders onto a 15HM low alloy steel substrate, leading to the following key findings:

- The interfacial solidification mode of the STT coating initiated with planar growth and concluded with dendritic growth. In contrast, the CXT coating's interfacial solidification mode began with cellular dendritic growth, progressed to planar growth, and ended with dendritic growth.
- Finite element analyses revealed distinct thermal distributions at the interfaces, with higher heat retention observed in the CXT specimen than in the STT specimen. This discrepancy resulted in unique observations: peninsula-like macrosegregations at the interface of the STT specimen and type-II boundaries at the interface of the CXT specimen.
- The STT coating exhibited faster cooling rates and a reduced average dendrite arm spacing (DAS) of 11.42 µm, in contrast to the CXT coating, having an average DAS of 15.56 µm.
- Grain size and crystallographic analyses, conducted using EBSD and XRD, revealed significant grain refinement in the STT coating. This refinement correlated with identified strengthening phases – γ-Ni, $Cr_{23}C_6$, and Cr_3C_2.
- Corrosion resistance tests, employing open circuit potential and electrochemical impedance spectroscopy, conclusively demonstrated superior corrosion resistance of the STT coating over the CXT coating.
- Additionally, hardness and wear resistance tests affirmed the superior mechanical properties of the STT coating, with higher hardness and a lower wear rate compared to the CXT coating.

CRediT authorship contribution statement

Augustine Nana Sekyi Appiah: Writing – review & editing, Writing – original draft, Methodology, Investigation, Formal analysis, Data curation, Conceptualization. **Gilmar Ferreira Batalha:** Writing – review & editing, Supervision, Methodology, Conceptualization. **Marcin Adamiak:** Writing – review & editing, Supervision, Resources, Methodology, Conceptualization.

Declaration of competing interest

The authors declare that they have no known competing financial interests or personal relationships that could have appeared to influence the work reported in this paper.

Data availability

Data will be made available on request.

Acknowledgment

The authors would like to show appreciation to The Silesian University of Technology with support through the Excellence Initiative - Research University grant number 32/014/RGJ24/2018.

Appendix A. Supplementary material

Supplementary data to this article can be found online at https://doi.org/10.1016/j.apsusc.2024.160320.

References

[1] Y. Wang, et al., A novel Al-Cr-Sc-Zr alloy additively manufactured via laser directed energy deposition: microstructure, phase analysis and mechanical properties, J. Mater. Process. Technol. 322 (2023) 118204, https://doi.org/10.1016/j.jmatprotec.2023.118204.

[2] S. Dong, B. Xu, Z. Lu, S. Chen, F. Jiang, Effect of plasma main arc on droplet transfer in skew-coupling arc welding, J. Mater. Process. Technol. 285 (2020) 116799, https://doi.org/10.1016/j.jmatprotec.2020.116799.

[3] T.G. Degefa, A. Wróbel, M. Płaczek, Modelling and study of the effect of geometrical parameters of piezoelectric plate and stack, Appl. Sci. 11 (24) (2021) 11872.

[4] L. Liu, et al., Marangoni flow patterns of molten pools in multi-pass laser cladding with added nano-CeO2, Addit. Manuf. 59 (2022) 103156, https://doi.org/10.1016/j.addma.2022.103156.

[5] Y.H. Kim, M.A. Rahman, J.S. Hwang, H. Ko, J.-Y. Huh, J.Y. Byun, Reflection color tuning of a metal–insulator–metal cavity structure using arc plasma deposition of gold nanoparticles, Appl. Surf. Sci. 562 (2021) 150140, https://doi.org/10.1016/j.apsusc.2021.150140.

[6] M. Adamiak, A.N.S. Appiah, R. Żelazny, G.F. Batalha, A. Czupryński, Experimental comparison of laser cladding and powder plasma transferred Arc welding methods for depositing wear-resistant NiSiB+ 60% WC composite on a structural-steel substrate, Materials 16 (11) (2023) 3912.

[7] K.A. Habib, et al., Effects of thermal spraying technique on the remelting behavior of NiCrBSi coatings, Surf. Coat. Technol. 444 (2022) 128669, https://doi.org/10.1016/j.surfcoat.2022.128669.

[8] Q. Wang, Q. Li, F.Q. Chen, L. Zhang, J.D. Li, J.W. Zhang, Corrosion behavior of laser-cladding NiCrBSi coating in molten aluminum alloy, J. Laser Appl. 34 (2) (2022).

[9] S. Wanare, V. Kalyankar, Influence of Fe dilution and W dissolution on abrasive wear resistance of NiCrBSi–WC composite hardfacing deposited by plasma transferred arc hardfacing, J. Adv. Manuf. Syst. 21 (04) (2022) 695–710.

[10] W. Liu, F. Guo, S. Liang, X. Wang, C. Shang, Evolution of M7C3 carbides near the solidus and the influence of Mn element on the formation of M23C6 carbides in a high carbon martensitic stainless steel 90Cr18MoV, Mater. Charact. 205 (2023) 113336.

[11] M. Ren, R. Li, X. Zhang, J. Gu, C. Jiao, Effect of WC particles preparation method on microstructure and properties of laser cladded Ni60-WC coatings, J. Mater. Res. Technol. 22 (2023) 605–616.

[12] Z. Chen, W. Li, L. Wang, X. Wei, Z. Liu, Investigation on the hot crack sensitivity of a nickel-based single crystal superalloy fabricated by epitaxial laser metal forming, J. Alloy. Compd. 931 (2023) 167436.

[13] L.A. Luiz, J. de Andrade, C.M. Pesqueira, I.B. de, A.F. Siqueira, G.B. Sucharski, M. J. de Sousa, Corrosion behavior and galvanic corrosion resistance of WC and Cr3C2 cermet coatings in madeira river water, J. Therm. Spray Technol. 30 (1–2) (2021) 205–221.

[14] S. Kim, et al., Improvement of hydrogen embrittlement by void formation at coating layers of Sb-added Al-Si-coated hot-press-forming steels, Corros. Sci. (2023) 111358.

[15] Y. Ge, M. Vronka, P. Veřtát, M. Karlik, S. Hannula, O. Heczko, Deformation twinning with different twin-boundary mobility in 2H martensite in Cu–Ni–Al shape memory alloy, Acta Mater. 226 (2022) 117598.

[16] L. Dong, Z. Shi, Y. Zhang, S. Wang, Q. Wang, L. Liu, Microstructure and sulfide stress corrosion cracking of the Inconel 625/X80 weld overlay fabricated by cold metal transfer process, Int. J.Hydrog. Energy 47 (67) (2022) 29113–29130, https://doi.org/10.1016/j.ijhydene.2022.06.210.

[17] Y. Zheng, et al., A numerical model-based deposition strategy for heat input regulation during plasma arc-based additive manufacturing, Addit. Manuf. 58 (2022) 102986, https://doi.org/10.1016/j.addma.2022.102986.

[18] F.W.C. Farias, et al., In situ interlayer hot forging arc plasma directed energy deposition of Inconel® 625: microstructure evolution during heat treatments, J. Alloy. Compd. 952 (2023) 170059, https://doi.org/10.1016/j.jallcom.2023.170059.

[19] X. Jia, et al., Plasma transferred Arc powder surfacing for titanium-clad steel plate, J. Therm. Spray Technol. (2023) 1–12.

[20] A.N.S. Appiah, O. Bialas, A. Czupryński, M. Adamiak, Powder plasma transferred Arc welding of Ni-Si-B+ 60 wt% WC and Ni-Cr-Si-B+ 45 wt% WC for surface cladding of structural steel, Materials 15 (14) (2022) 4956.

[21] A. Czupryński, Microstructure and abrasive wear resistance of metal matrix composite coatings deposited on steel grade AISI 4715 by powder plasma transferred arc welding part 1. mechanical and structural properties of a cobalt-based alloy surface layer reinforced with particles of titanium carbide and synthetic metal–diamond composite, Materials 14 (9) (2021) 2382.

[22] Y. Fu, et al., Fe–Co-based crystalline soft magnetic coatings with ultra-high saturation magnetization above 1.9 T via co-axial powder feeding plasma-transferred arc welding, J. Mater. Sci. Mater. Electron. 34 (6) (2023) 468.

[23] V. ArunKumar, N. Prakash, K. Deenadayalan, Comparison between the spherical and angular type WC particles reinforced in Nickel-based matrix deposited using plasma transferred Arc welding process, Mater. Today:. Proc. (2023), https://doi.org/10.1016/j.matpr.2023.02.344.

[24] P. Gao, et al., Preparations of iron-based alloy coatings on grey cast iron through plasma transfer arc welding, J. Adhes. Sci. Technol. 36 (8) (2022) 833–844.

[25] C. Wang, et al., A simplified modelling approach for thermal behaviour analysis in hybrid plasma arc-laser additive manufacturing, Int. J. Heat Mass Transf. 195 (2022) 123157.

[26] P. Kumar, N.K. Jain, M.S. Sawant, Development of theoretical models for dimensions of single-layer multi-track and multi-layer multi-track depositions by μ-PTA additive manufacturing process, J. Mater. Res. Technol. 17 (2022) 95–110.

[27] X. Chen, C. Wang, J. Ding, P. Bridgeman, S. Williams, A three-dimensional wire-feeding model for heat and metal transfer, fluid flow, and bead shape in wire plasma arc additive manufacturing, J. Manuf. Process. 83 (2022) 300–312.

[28] Y. Gao, Z. Yang, H. Xiao, Q. Lei, B. Liu, Y. Liu, Effect of welding current on wear behavior of PTA-welded Cu35Ni25Co25Cr15 HEA coating, Coatings 13 (1) (2022) 52.

[29] A.G. Momin, B.C. Khatri, U. Shah, J. Valaki, Parameters for cladding using plasma transfer arc welding–a critical, Mater. Today:. Proc. 77 (2023) 614–618.

[30] K. Kishore, N. Jaiswal, A. Prabhakaran, K.S. Arora, Through-thickness microstructure and wear resistance of plasma transferred arc Stellite 6 cladding: effect of substrate, CIRP J. Manuf. Sci. Technol. 42 (2023) 24–35.

[31] P.H.G. Dornelas, T.G. Santos, J.P. Oliveira, Micro-metal additive manufacturing–state-of-art and perspectives, Int. J. Adv. Manuf. Technol. 122 (9–10) (2022) 3547–3564.

[32] E. Tan Zhi'En, J. H. L. Pang, and J. Kaminski, "Directed energy deposition build process control effects on microstructure and tensile failure behaviour," *J. Mater. Process. Technol.*, 294, p. 117139, 2021, doi: 10.1016/j.jmatprotec.2021.117139.

[33] M. Moradi, A. Hasani, Z. Pourmand, J. Lawrence, Direct laser metal deposition additive manufacturing of Inconel 718 superalloy: statistical modelling and optimization by design of experiments, Opt. Laser Technol. 144 (2021) 107380, https://doi.org/10.1016/j.optlastec.2021.107380.

[34] Z. Yang, et al., Effects of ultrasound on multilayer forming mechanism of Inconel 718 in directed energy deposition, Addit. Manuf. 48 (2021) 102462, https://doi.org/10.1016/j.addma.2021.102462.

[35] Z. Mao, X. Lu, H. Yang, X. Niu, L. Zhang, X. Xie, Processing optimization, microstructure, mechanical properties and nanoprecipitation behavior of 18Ni300 maraging steel in selective laser melting, Mater. Sci. Eng. A 830 (2022) 142334, https://doi.org/10.1016/j.msea.2021.142334.

[36] D. Roucou, T. Corre, G. Rolland, V. Lazarus, Effect of the deposition direction on fracture propagation in a duplex stainless steel manufactured by directed energy deposition, Mater. Sci. Eng. A 878 (2023) 145176, https://doi.org/10.1016/j.msea.2023.145176.

[37] J.-H. Kim, C.-M. Lee, D.-H. Kim, The effect of plasma-assisted machining and additive path strategies of Inconel 718 manufactured with directed energy deposition, J. Mater. Res. Technol. 19 (2022) 1658–1672, https://doi.org/10.1016/j.jmrt.2022.05.108.

[38] Y.A. Gueche, et al., Selective laser sintering of solid oral dosage forms with copovidone and paracetamol using a CO2 laser, Pharmaceutics 13 (2) (2021) 160.

[39] A. Raza, C. Pauzon, S. Dubiez-Le Goff, and E. Hryha, Effect of processing gas on spatter generation and oxidation of TiAl6V4 alloy in laser powder bed fusion process, *Appl. Surf. Sci.*, vol. 613, p. 156089, 2023, doi: 10.1016/j.apsusc.2022.156089.

[40] F. Bjørheim, D.G. Pavlou, S.C. Siriwardane, Nonlinear fatigue life prediction model based on the theory of the S-N fatigue damage envelope, Fatigue Fract. Eng. Mater. Struct. 45 (5) (2022) 1480–1493.

[41] A. Przyłucka-Bednarska, M. Rywotycki, K. Sołek, Z. Malinowski, The heaT transfer process BeTween two bodies wiTh a Large TemPeraTure difference, Arch. Metall. Mater. (2022) 1161–1165.

[42] O. Dvirna, N. Zembrzuska, Technological methods of ensuring the reliability of lock connections in marine gas turbines, J. Konbin 52 (3) (2022) 149–164.

[43] M.I. Al Hamahmy, I. Deiab, Review and analysis of heat source models for additive manufacturing, Int. J. Adv. Manuf. Technol. 106 (2020) 1223–1238.

[44] P. Jiang, S. Gao, S. Geng, C. Han, G. Mi, Multi-physics multi-scale simulation of the solidification process in the molten pool during laser welding of aluminum alloys, Int. J. Heat Mass Transf. 161 (2020) 120316.

[45] D. StJohn, A. Prasad, M. Easton, M. Qian, The contribution of constitutional supercooling to nucleation and grain formation, Metall. Mater. Trans. A 46 (2015) 4868–4885.

[46] P. Liang, et al., Highly reversible Zn anode enabled by controllable formation of nucleation sites for Zn-based batteries, Adv. Funct. Mater. 30 (13) (2020) 1908528.

[47] S. Sudhagar, M. Sakthivel, P. Ganeshkumar, Monitoring of friction stir welding based on vision system coupled with Machine learning algorithm, Measurement 144 (2019) 135–143.

[48] C. Wang, Y. Yu, J. Yu, Y. Zhang, F. Wang, H. Li, Effect of the macro-segregation on corrosion behavior of CrMnFeCoNi coating prepared by arc cladding, J. Alloy. Compd. 846 (2020) 156263.

[49] G. Prabu, M. DuraiselvaM, Tribological studies on AlCrFeCuCoNi high entropy alloy surface coated on Ti-6Al-4V using plasma transferred arc technique, Arch. Metall. Mater. (2022) 409–420.

[50] X. Zhang, Y. Komizo, In situ investigation of the allotropic transformation in iron, Steel Res. Int. 84 (8) (2013) 751–760.

[51] B. Wang, L. Ouyang, J. Xu, P. Huang, E. Liu, B. Yang, Study on stress corrosion cracking behavior of incoloy825/X65 bimetallic composite pipe welded joint in wet hydrogen sulfide environment, Metals 12 (4) (2022) 632.

[52] L. Quintino, "Overview of coating technologies," in *Surface Modification by Solid State Processing*, Elsevier, 2014, pp. 1–24.

[53] A.-W.-Y. Tan, et al., Microstructure, mechanical and tribological properties of cold sprayed Ti6Al4V–CoCr composite coatings, Compos. B Eng. 202 (2020) 108280, https://doi.org/10.1016/j.compositesb.2020.108280.
[54] A. Caprì, A. Frazzica, L. Calabrese, Recent developments in coating technologies for adsorption heat pumps: a review, Coatings 10 (9) (2020) 855.
[55] T.A. Passos, H. Costa, F.K.C. Luz, G. Pintaude, The effect of the dilution level on microstructure and wear resistance of Fe-Cr-CV hardfacing coatings deposited by PTA-P, Coatings 12 (12) (2022) 1835.
[56] C. Gu, C.D. Ridgeway, M.P. Moodispaw, A.A. Luo, Multi-component numerical simulation and experimental study of dendritic growth during solidification processing, J. Mater. Process. Technol. 286 (2020) 116829, https://doi.org/10.1016/j.jmatprotec.2020.116829.
[57] A.N.S. Appiah, et al., Microstructure and performance of NiCrBSi coatings prepared by modulated arc currents using powder plasma transferred arc welding technology, Appl. Surf. Sci. 648 (2024) 159065, https://doi.org/10.1016/j.apsusc.2023.159065.
[58] K. Deenadayalan, V. Murali, A. Elayaperumal, S. Arulvel, Effective role of short time furnace heat treatment and laser treatment on the residual stress and mechanical properties of NiCrBSi–WC weldments produced using plasma transferred arc welding process, J. Mater. Res. Technol. 15 (2021) 3492–3513, https://doi.org/10.1016/j.jmrt.2021.09.113.
[59] L.-Y. Chen, et al., Phase interaction induced texture in a plasma sprayed-remelted NiCrBSi coating during solidification: an electron backscatter diffraction study, Surf. Coat. Technol. 358 (2019) 467–480, https://doi.org/10.1016/j.surfcoat.2018.11.019.
[60] A.N.S. Appiah, et al., Vanadium-induced structural effects on the corrosion and tribological properties of an Al-Li binary alloy, J. Alloy. Compd. 973 (Feb. 2024) 172910, https://doi.org/10.1016/j.jallcom.2023.172910.
[61] B. Wu, et al., Effects of synchronized magnetic arc oscillation on microstructure, texture, grain boundary and mechanical properties of wire arc additively manufactured Ti6Al4V alloy, Addit. Manuf. 54 (2022) 102723, https://doi.org/10.1016/j.addma.2022.102723.
[62] L. Monier, et al., On the origin of grain refinement and twin boundaries in as-fabricated austenitic stainless steels produced by laser powder bed fusion, Addit. Manuf. 61 (2023) 103351, https://doi.org/10.1016/j.addma.2022.103351.
[63] A. Issariyapat, P. Visuttipitukul, J. Umeda, K. Kondoh, Refined grain formation behavior and strengthening mechanism of α-titanium with nitrogen fabricated by selective laser melting, Addit. Manuf. 36 (2020) 101537, https://doi.org/10.1016/j.addma.2020.101537.
[64] Y. Zhao, et al., Significant reduction of grain size and texture intensity in laser powder bed fusion fabricated nickel-based superalloy by increasing constitutional supercooling, Compos. B Eng. 266 (2023) 111040, https://doi.org/10.1016/j.compositesb.2023.111040.
[65] L. Xu, et al., Low-temperature densification of high entropy diboride based composites with fine grains and excellent mechanical properties, Compos. B Eng. 247 (2022) 110331, https://doi.org/10.1016/j.compositesb.2022.110331.
[66] C.H. Ng, M.J. Bermingham, M.S. Dargusch, Eliminating porosity defects, promoting equiaxed grains and improving the mechanical properties of additively manufactured Ti-22V-4Al with super-transus hot isostatic pressing, Addit. Manuf. 72 (2023) 103630, https://doi.org/10.1016/j.addma.2023.103630.
[67] B. Chang, Z. Yi, L. Duan, F. Zhang, J. Duan, Surface wear resistance and microstructure characteristic in longitudinal–torsional ultrasonic vibration side milling of GH4169 superalloy, Appl. Surf. Sci. 649 (2024) 159075, https://doi.org/10.1016/j.apsusc.2023.159075.
[68] Y. Tsutsumi, et al., Crystallographic texture- and grain boundary density-independent improvement of corrosion resistance in austenitic 316L stainless steel fabricated via laser powder bed fusion, Addit. Manuf. 45 (2021) 102066, https://doi.org/10.1016/j.addma.2021.102066.
[69] B. Wu, et al., Enhanced corrosion performance in Ti-6Al-4V alloy produced via wire-arc directed energy deposition with magnetic arc oscillation, Addit. Manuf. 66 (2023) 103465, https://doi.org/10.1016/j.addma.2023.103465.
[70] Y. Yang, X. Li, M.M. Khonsari, Y. Zhu, H. Yang, On enhancing surface wear resistance via rotating grains during selective laser melting, Addit. Manuf. 36 (2020) 101583, https://doi.org/10.1016/j.addma.2020.101583.
[71] C. Navas, R. Vijande, J.M. Cuetos, M.R. Fernández, J. de Damborenea, Corrosion behaviour of NiCrBSi plasma-sprayed coatings partially melted with laser, Surf. Coat. Technol. 201 (3) (2006) 776–785, https://doi.org/10.1016/j.surfcoat.2005.12.032.
[72] Y. Wang, et al., Effect of heat treatment temperature on the microstructure and wear corrosion properties of NiCrBSi–TiN composite coatings, Ceram. Int. 48 (5) (2022) 6933–6941, https://doi.org/10.1016/j.ceramint.2021.11.249.
[73] M.W.A. Rashid, M. Gakim, Z.M. Rosli, M.A. Azam, Formation of Cr23C6 during the sensitization of AISI 304 stainless steel and its effect to pitting corrosion, Int. J. Electrochem. Sci. 7 (10) (2012) 9465–9477, https://doi.org/10.1016/S1452-3981(23)16211-0.
[74] S. Wu, Y. Fei, B. Guo, L. Jing, Corrosion of Cr23C6 coated Q235 steel in wet atmospheres containing Na2SO4 at 750°C, Corros. Sci. 100 (2015) 306–310, https://doi.org/10.1016/j.corsci.2015.08.008.
[75] M. Somervuori, T. Varis, M. Oksa, T. Suhonen, P. Vuoristo, Comparative study on the corrosion performance of APS-, HVOF-, and HVAF-sprayed NiCr and NiCrBSi coatings in NaCl solutions, J. Therm. Spray Technol. 31 (5) (2022) 1581–1597.
[76] F. da C. Gallo, L. M. B. de Azevedo, C. Labre, L. S. Araújo, J. Dille, and L. H. de Almeida, Correlation between grain boundary character distribution and δ-phase precipitation in nickel-based superalloy 718, *J. Mater. Res. Technol.*, 9 (2) pp. 1801–1808, 2020, doi: 10.1016/j.jmrt.2019.12.011.
[77] R.B. Figueiredo, M. Kawasaki, T.G. Langdon, Seventy years of Hall-Petch, ninety years of superplasticity and a generalized approach to the effect of grain size on flow stress, Prog. Mater. Sci. (2023) 101131.
[78] J. Xie, C. Cai, Y. Liang, Z. Liu, Y. Ma, Microstructure and mechanical properties of heat affected zone of laser-MAG hybrid welded low carbon bainitic steel joints, Opt. Laser Technol. 148 (2022) 107729.
[79] Y. Lanoiselée, A. Stanislavsky, D. Calebiro, A. Weron, Temperature and friction fluctuations inside a harmonic potential, Phys. Rev. E 106 (6) (2022) 064127.
[80] M. Varenberg, Adjusting for running-in: extension of the archard wear equation, Tribol. Lett. 70 (2) (2022) 59.
[81] J. Zhou, et al., Preparation of NiCrBSi-WC/Co coatings by stable magnetic field assisted supersonic plasma spraying and its wear resistance mechanism, Mater. Charact. 194 (2022) 112433, https://doi.org/10.1016/j.matchar.2022.112433.